Thermodynamic properties of minerals and fluids

Brichkina E.A., Voronin M.V., Osadchiy E.G. Thermodynamic properties of krennerite ($AgAu_3Te_8$) and silvanite ($AgAuTe_4$): experimental determination by the EMF method *UDC 544.31*

D.S. Korzhinskii Institute of Experimental Mineralogy of Russian Academy of Sciences *e-mail: brichkina@iem.ac.ru*

Abstract. The thermodynamic properties of reactions involving krennerite ($AgAu_3Te_8$) and sylvanite ($AgAuTe_4$) were determined by measuring electromotive forces (EMF) using a solid electrolyte Ag_4RbI_5 (up to 500 K) in the Ag-Au-Te system in the temperature range 332K - 485K. The dependences E(T) were obtained in all-solid-state electrochemical cells with a common gas space in accordance with the following reactions:

$Ag + 2Te + 3AuTe_2 = AgAu_3Te_8$
$3Ag+4Te+AgAu_3Te_8=3AgAuTe_4$
Using the reference data, the standard (298.15 K, 1 bar (10^5 Pa)) thermodynamic properties (Δ_fG^0, ΔS^0, Δ_fH^0) of krennerite and sylvanite formation from the elements were calculated: $\Delta_fG^0(AgAu_3Te_8)$ = -78.11 kJ·mol^{-1}; $S^0(AgAu_3Te_8)$ = 580.6 J·mol^{-1}·K^{-1}; $\Delta_fH^0(AgAu_3Te_8)$ = -78.26 kJ·mol^{-1} and sylvanite: Δ_fG^0 ($AgAuTe_4$) = -51.22 kJ·mol^{-1}; $S^0(AgAuTe_4)$ = 326.59 J·mol^{-1}·K^{-1}; Δ_fH^0 ($AgAuTe_4$) = -79.83 kJ·mol^{-1}.

Keywords: sylvanite, $AgAuTe_4$, krennerite, $AgAu_4Te_{10}$, $AgAu_3Te_8$, electromotive force method, Ag-Au-Te system.

Introduction

Tellurides of gold and silver are not widespread in nature, but are important gold minerals for gold mining. Knowledge of the thermodynamic properties of minerals is necessary for the physicochemical interpretation of chalcogenide gold-silver deposit paragenesis, such as: determining the forms of transfer and deposition of ore components, studying the geochemical parameters of the formation of ore paragenesis and mineral associations. No thermodynamic data were found in the literature for compounds corresponding to the formulas of the minerals krennerite and sylvanite.

The study and analysis of literature data on the compositions of natural samples of krennerite and sylvanite was carried out in (Dye and Smyth, 2012), where in krennerite grains the Ag content varied from 6.26 to 8.04 at.% (7.14 at.% on average) and in sylvanite grains the Ag content from 9.03 to 11.93 at.% (average 10.48 at.%). Microprobe analyzes are consistent with the data obtained using X-ray diffraction, the average empirical formula of krennerite is $Au_{2.9}Ag_{0.9}Te_8$. Microprobe data for sylvanite show that its average empirical formula is $Au_{1.3}Ag_{0.6}Te_4$. The microprobe analysis data obtained in (Dye and Smyth, 2012) did not reveal any superposition of krennerite and sylvanite compositions, which is consistent with the experimental data of Cabri (Cabri, 1965).

Theoretical justification of measurements

The Gibbs energy value is calculated from the temperature dependence of the electromotive force corresponding to the electrochemical process of the compound formation reaction, which is written for krennerite as follows:

$Ag = Ag^+ + e^-$ left electrode (reference system),

$Ag^+ + e^- + 2Te + 3AuTe_2 = AgAu_3Te_8$ right electrode (sample system),

---

$Ag + 2Te + 3AuTe_2 = AgAu_3Te_8$ total potential-forming reaction (R1)

Reaction (R1) was implemented in an electrochemical cell:

(–)Pt| C(graphite) | Ag | $RbAg_4I_5$ | Te, $AuTe_2$, $AgAu_3Te_8$ | C(graphite) | Pt (+) (A)

To determine the Gibbs energy of sylvanite formation:

$3Ag = 3Ag^+ + 3e^-$ left electrode (comparison system),

$3Ag^+ + 3e^- + 4Te + AgAu_3Te_8 = 3AgAuTe_4$ right electrode (sample system),

---

$3Ag + 4Te + AgAu_3Te_8 = 3AgAuTe_4$ total potential-forming reaction (R2)

The reaction (R2) is implemented in an electrochemical cell:

(–)Pt| C(graphite) | Ag | $RbAg_4I_5$ | Te, $AgAuTe_4$, $AgAu_3Te_8$ | C(graphite) | Pt(+) (B)

Experimental part

Reagents. The phases were synthesized using Te powder (99.9999%) obtained by zone melting, gold (99.99%), and silver (99.99%) in the form of sheets 0.2 mm thick. The solid electrolyte $RbAg_4I_5$ (99.99%) was prepared at the Institute of Microelectronics Technology and High-Purity Materials of the Russian Academy of Sciences (Chernogolovka).

Phase synthesis. The sample systems for the electrochemical cell were synthesized from elemental Ag, Au and Te according to the Cabri diagram (Cabri, 1965). The mixtures were synthesized at a temperature of 500 °C for a day, then homogenizing grinding and annealing at 300 °C, grinding and annealing at 230 °C were performed again.

The phase compositions of the samples before and after the experiment were confirmed by X-ray phase analysis: map #85-1310 for $AuTe_2$ (Schutte and De Boer, 1988), #75-1413 for $AgAu_3Te_8$ (Pertlik, 1984a), $AgAuTe_4$ # 01-073-2879 (Tunnel, 1941) and Te #00-004-0555 (Swanson, 1953).

Manufacturing of EMF components of the cell. Inert electrodes were made from a graphite rod for spectral analysis with a diameter of 6 mm, which were connected to a platinum wire. The electrode of the reference system was a silver pellet ~6 mm in diameter and 3 mm high.

Polycrystalline $RbAg_4I_5$ was used as a solid electrolyte. Approximately 0.4 grams of electrolyte in the form of a powder was pressed at a load of 2.5 tons into a tablet 6 mm in diameter and 3 mm high.

To fabricate electrodes of the sample system, mixtures of $AuTe_2$, $AgAu_3Te_8$, Te and Te, $AgAuTe_4$, $AgAu_3Te_8$ were ground (homogenized) in an agate mortar and pressed under a load of 2.5 tons into tablets ~6 mm in diameter and 3–4 mm high.

Galvanic cell device. The cell was assembled in a cell holder in the form of a quartz glass tube (internal diameter ~6.1 mm). A detailed description of the experimental setup with solid electrolytes and the procedure for working with it are given in (Voronin, Osadchii, 2011). The measurements were carried out in a flow of dry argon (2-3 $cm^3 \cdot min^{-1}$) to prevent oxidation of cell parts.

Results of EMF measurements

The experimental values of E(T) obtained in the heating and cooling modes of cells (A) and (B) are shown in **Table 1** and **Figure 1**.

Table 1. Experimental values of E(T) for:
a) cell (A) and b) cell (B).

a) **K 577**

T, K	E,mV	T, K	E,mV	T, K	E,mV
466.00	291.88	360.66	282.75	422.74	288.34
447.17	290.65	351.25	281.56	432.41	288.99
437.62	289.90	355.84	282.27	441.96	289.59
418.37	288.06	365.13	283.22	446.69	289.94
408.50	287.45	374.40	284.15	461.16	290.79
398.88	286.44	383.90	285.14	465.85	291.45
389.19	285.69	393.50	286.00	470.59	292.26
379.50	284.54	403.01	286.86		
370.05	283.66	412.96	287.54		

b) **K 578**

T, K	E,mV	T, K	E,mV	T, K	E,mV
494.15	280.15	483.92	280.90	379.96	275.14
474.19	279.82	473.91	280.74	385.01	275.73
464.19	279.84	453.96	280.51	390.06	276.92
454.16	279.58	443.93	280.12	395.11	277.60
444.21	279.18	433.79	279.83	400.20	277.96
423.89	278.63	423.63	279.34	405.36	278.77
439.07	279.53	413.38	278.87	410.54	279.18
449.16	279.97	403.03	278.29	410.54	279.17
459.07	280.14	392.88	277.46	415.64	279.56
469.02	280.41	382.82	276.58	420.81	279.89
478.99	280.47	372.95	274.18		

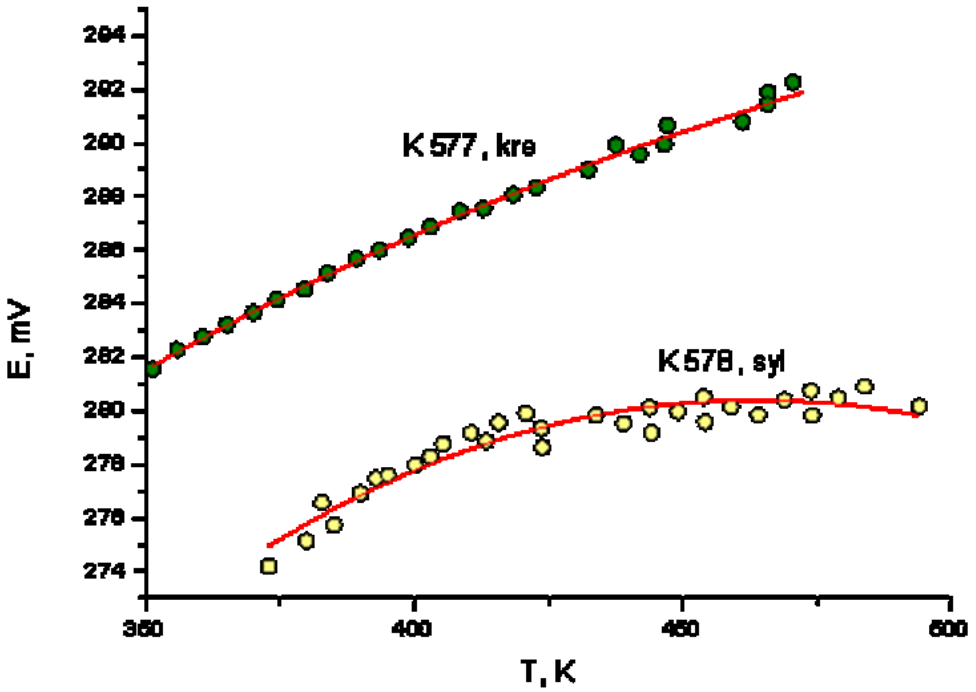

Figure 1. Temperature dependence of the EMF of cells (A) and (B).

E(T) dependences have the form of a smooth curve and are described by logarithmic equations:

E(A), mV = 176.61 + 1.3928·T – 0.18658·T·ln(T),

K 577, (350 < T/K < 470), k = 25, R^2 = 0.99571 (1)

E(B), mV = 15.12 + 4.0844·T – 0.5721·T·ln(T),

K 578, (370 < T/K < 490), k = 32, R2 = 0.90444 (2)

For the equations, the temperature range of measurements, the number of experimental E/T points (k) and the coefficient of determination (R2) are given. Knowing the temperature dependence of the EMF of the cell and using the basic equations of thermodynamics, the following thermodynamic functions can be determined:

$\Delta_r G$ (J·mol^{-1}) = -nFE×10^{-3}

$\Delta_r S$ (J·K^{-1}·mol^{-1}) = nF·(dE/dT)×10^{-3}

$\Delta_r H$ (J·mol^{-1}) = -nF·[E - (dE/dT)·T]×10^{-3}

where n = 1 or 3 is the number of electrons involved in the reaction (R1) or (R2), F= 96485.33289 C·mol^{-1} is the Faraday constant, and E is the EMF in millivolts.

Using auxiliary data for elements and calaverite taken from (Barin, 1995) (**Table 2**), the standard thermodynamic properties of the formation of krennerite $AgAu_3Te_8$ and sylvanite $AgAuTe_4$ from elements at a pressure of 1 bar (10^5 Pa) were calculated: (10^5 Па): $\Delta_f G^0(AgAu_3Te_8)$ = -78.11 kJ·mol^{-1}; $S^0(AgAu_3Te_8)$ = 580.6 J·mol^{-1}·K^{-1}; $\Delta_f H^0(AgAu_3Te_8)$ = -78.26 kJ·mol^{-1} and of sylvanite: $\Delta_f G^0$ ($AgAuTe_4$) = -51.22 kJ·моль$^{-1}$; $S^0(AgAuTe_4)$ = 326.59 J·mol^{-1}·K^{-1}; $\Delta_f H^0$ ($AgAuTe_4$) = -79.83 kJ·mol^{-1}.

Table 2. Standard thermodynamic values of krennerite and auxiliary data for elements and $AuTe_2$ at 298.15 K and 1 bar.

Substance	$\Delta_f G°$ (kJ·mol^{-1})	S° (J·mol^{-1} K^{-1})	$\Delta_f H°$ (kJ·mol^{-1})	note (reference)
Ag	0	42.677	0	Barin, 1995
Au	0	47.497	0	–//–
Te	0	49.497	0	–//–
$AuTe_2$	-17.194	141.712	-18.619	–//–
$AgAu_3Te_8$	-78.11	580.6	-78.26	reaction (R1)
$AgAuTe_4$	-51.22	326.59	-79.83	reaction (R2)

Acknowledgments: The authors thank N.A. Drozhzhina for XRD analyses.

References

Barin I. (1995). Thermochemical data of pure substances // VCH-Verlag-Ges.,V. 1 and 2.

Cabri L.J. (1965) Phase relations in the Au-Ag-Te systems and their mineralogical significance // Economic Geology, V. 60, No. 8, P. 1569-1606.

Dye M.D., Smyth J.R. (2012). The crystal structure and genesis of krennerite, Au_3AgTe_8 // The Canadian Mineralogist, V. 50, No. 1, P. 119-127.

Kitahara G., Yoshiasa A., Tokuda M., Nespolo M., Hongu H., Momma K., Miyawakid R., Sugiyama K. (2022) Crystalstructure, XANES and charge distribution investigation of krennerite and sylvanite: analysis of Au-Te and Te-Te bonds in Au1- xAg_xTe_2 group minerals // ActaCryst. B 78, P.117–132.

Pertlik F. (1984a). Crystal chemistry of natural tellurides II: Redetermination of the crystal structure of krennerite, $(Au_{1-x}Ag_x)Te_2$ with x∼0.2 // Tschermaks Mineralogische und Petrographische Mitteilungen, V. 33, No 4, P. 253-262.

Pertlik, F. (1984b). Crystal chemistry of natural tellurides. I: Refinement of the crystal structure of sylvanite, $AuAgTe_4$ // Tschermaks mineralogische und petrographische Mitteilungen, V. *33*, P. 203-212.

Schutte W.J., De Boer J.L. (1988). Valence fluctuations in the incommensurately modulated structure of calaverite $AuTe_2$ // Acta Crystallographica Section B: Structural Science, V. 44, No. 5, P. 486-494.

Swanson T. (1953) Standard X-ray Diffraction Powder Patterns // Natl. Bur. Stand. (U.S.), Circ. 539, V. 1, P. 26.

Tunell G. (1941). The atomic arrangement of sylvanite // American Mineralogist V.26, No 8, P. 457–477.

Voronin M.V., Osadchii E.G. (2011) Determination of thermodynamic properties of silver selenide by the galvanic cell method with solid and liquid electrolytes // Russian Journal of Electrochemistry, V. 47, P. 420-426.

Voronin M.V., Osadchiy E.G., Brichkina E.A., Osadchiy V.O. (2022) Determination of the thermodynamic properties of krennerite ($AgAu_4Te_{10}$ or $AgAu_3Te_8$) by the EMF method with a solid electrolyte Ag_4RbI_5 // Abstracts of the All-Russian Annual Seminar on Experimental Mineralogy, Petrology and Geochemistry (VESEMPG-2022), Moscow, April 19-20, 2022, GEOKHI RAS Moscow, P. 216–219 (in Russian).

Persikov E.S.[1], Bukhtiyarov P.G.[1], Shaposhnikova O.Y.[1], Aranovich L.Ya.[2], Nekrasov A.N.[1], Kosova S.A.[1] Features of crystallization of andesite melt at moderate hydrogen pressures (experimental study)

UDC 552.11

[1] IEM RAS [2] IGEM RAS persikov@iem.ac.ru.

Abstract. Important problems of magma differentiation, the formation of native metals and ore formation processes in the earth's crust are increasingly associated with the active participation of hydrogen. In this paper, new experimental data on the crystallization of andesitic melts at high temperatures (900 – 1250 ˚C) and hydrogen pressures (10-100 MPa) were obtained, which clarify the possible role of hydrogen in the processes occurring in andesite melts in the earth's crust and during volcanism in strongly recovered conditions (f(O_2) = 10^{-14}). In crystallization experiments, it was found that the compositions of crystals (pyroxenes and plagioclases) formed in the experiment on crystallization of andesite

melt under hydrogen pressure closely correspond to the compositions of crystals of lava flows of the Avacha volcano in Kamchatka. This result can be considered as an experimental confirmation of the participation of hydrogen in the volcanic process.

Keywords: andesite melt, hydrogen, pressure, temperature, native metal, crystallization, reducing conditions

The role of hydrogen, the most abundant element in our galaxy, in natural processes is extremely diverse and in recent years has attracted increasing attention from petrologists and geochemists. Including the problems of differentiation of magmas, the formation of native metals and the processes of ore formation in the earth's crust, are increasingly associated with the active participation of hydrogen (Bird et al., 1981; Ryabov et al., 1985; Oleynikov et al., 1985; Marakushev, 1995; Levashov and Okrugin, 1984; etc**.).** Recently, we obtained the first results on experimental modeling of the formation of native metals in the earth's crust during the interaction of hydrogen with basalt melts and on the kinetics of differentiation of basalt magma under hydrogen pressure (Persikov et al., 2019). In this work, new experimental data on the crystallization of andesite melts at high temperatures (900 - 1250 °C) and hydrogen pressures (10 - 100 MPa), which clarify the possible role of hydrogen in the processes occurring in andesite melts in the earth's crust and during volcanism under highly reducing conditions. The experiments were carried out using a unique high-gas pressure setup. This device is equipped with an original internal device, which made it possible to conduct long-term experiments at such high temperatures, despite the high penetrating power of hydrogen. This device is considered in detail in the work (Persikov et al., 2019, Fig. 1), here we will explain in a brief form. The device includes a molybdenum reactor with a molybdenum ampoule placed in it with an initial sample of remelted andesite (approximately 150 mg). The reactor is hermetically connected to the piston equalizer - separator. The internal volumes of the molybdenum reactor and the equalizer-separator under the piston were filled with hydrogen at a pressure of 10 MPa using a special system. The device assembled in this way, together with the internal heater, was placed inside a high-pressure vessel (IHPV) so that the ampoule with the andesite sample was in the gradient-free temperature zone of the heater. Due to the movement of the equalizer-separator piston, the hydrogen pressure in the internal volume of the molybdenum reactor was always kept equal to the gas pressure (Ar) in the vessel during the experiment. At the beginning of the experiment, the pressure of argon in the vessel and, accordingly, hydrogen in the reactor was raised for one hour to the required value of 100 MPa. Next, the temperature of the experiment was raised to the required value of 1250 °C. Withstand the specified parameters in automatic mode for 1 hour, then reduce the hydrogen pressure to 10 MPa in isothermal mode for 1 hour, hold for 1 hour, and then reduce the temperature to 1000 °C or 900 °C, exposure for 2 hours (crystallization), After that, isobaric hardening was carried out with the internal heater of the installation turned off. The quenching speed of the samples was ~ 300 °C / min. The error of measuring the temperature of the experiment was ± 5 °C, and the pressure of hydrogen ± 0.1 % rel. After isobaric quenching, pressure relief in the vessel and complete cooling, the internal device was removed from the high-pressure vessel, the ampoules with the sample were removed from the molybdenum reactor for subsequent analysis of the phases formed during the experiment. The experiments used natural samples of andesite of the volcano Avacha (Kamchatka). The chemical composition of the phases obtained in the experiments (Tabl. 1, 2) was determined using a digital electron X-ray microscope CamScan MV 2300 (VEGA TS 5130 MM), with an attachment for energy-dispersive microanalysis INCA Energy 450 and WDS Oxford INCA Wave 700. The analyses were carried out at an accelerating voltage of 20 kV with a beam current of up to 400 nA and a spectra-set time of 50-100 seconds.

To estimate the magnitude of oxygen fugacity corresponding to the cessation of redox reactions in andesite melts in crystallization experiments (No. 2157), equation (1) and the measured amounts of H_2O dissolved in the melt (0.21 wt. %, Tabl. 1).

$$f(O_2) = [f(H_2O)/ (f(H_2)\cdot\exp (- \Delta Go(1)/RT))]^2, \qquad (1)$$

Table 1. Chemical composition (wt. %) and structural-chemical parameter (100NBO/T) of the initial andesite (glass), minerals and melts (glass) after experiments under hydrogen pressure

Components	№ 2057 *	№ 2057 **	№ 2057 ***	№ 2058 ****	№ 2058 *****	№ 2058 ******	Composition of the original andesite (glass)
SiO_2	62.75	48.65	65.69	60.44	67.14	51.74	58.8
Al_2O_3	17.88	6.9	18.55	16.3	18.43	13.93	16.62
Fe_2O_3	0.00	0.00	0.00	0.0	0.0	0.0	1.0
FeO	2.86	10.99	2.96	4.35	2.15	5.44	5.66
MnO	0.23	0.16	0.33	0.15	0.13	0.27	0.11
MgO	1.85	29.95	1.39	5.47	0.67	13.85	5.59
CaO	7.34	3.32	4.43	7.29	4.18	12.54	6.77
Na_2O	4,89	1.18	4.0	4.03	4.42	1.25	4.15
K_2O	1.54	0.49	1.84	1.26	1.88	0.33	1.32
TiO_2	0.66	0.12	0.81	0.68	1.0	0.6	0.59
$P2O_5$	0.18	0.15	н. о.	н. о.	0.0	0.0	0.20
H_2O^+	-	-	-	-	0.0	0.0	-
H_2O^-	0.21	0.00	-	0.37	0.0	0.0	0.11
Sum	100	101.75	100	100.37	100	100	100
100NBO/T	**26.6**	**191**	**20.1**	**30.6**	**22.4**	**96**	**39.1**

Note:

* - glass, $P(H_2)$ = 100 MPa, T = 1250 °C, holding for 1 hour, then reducing the hydrogen pressure to 10 MPa in isothermal mode for 1 hour, holding for 1 hour, and then lowering the temperature to 1000 °C, holding for 2 hours (crystallization) and then isobaric quenching; ** - pyroxene crystals; *** - plagioclase; **** - glass, the parameters of the experiment are the same, only the crystallization temperature is 900 °C; ***** - plagioclase; ****** - pyroxene crystals.

Table 2. Chemical compositions (wt. %) of metal phases in andesite melts (quenched samples) after experiments under hydrogen pressure

Components	№ 2157	№ 2158
Fe	98.07	98.88
Mg	0.84	0.08
Ti	0.08	0.15
O	1.2	0.7
Si	0.16	0.05
Ca	0.23	0.07
P	0.52	0.03
Sum	**101.1**	**99.96**

Note:

1. The results presented in the table are the averages of 7 measurements.
2. The concentrations of all impurity elements (Si, Ca, Ti, P) in the metal phases are determined approximately, since these values are within the analytical errors.

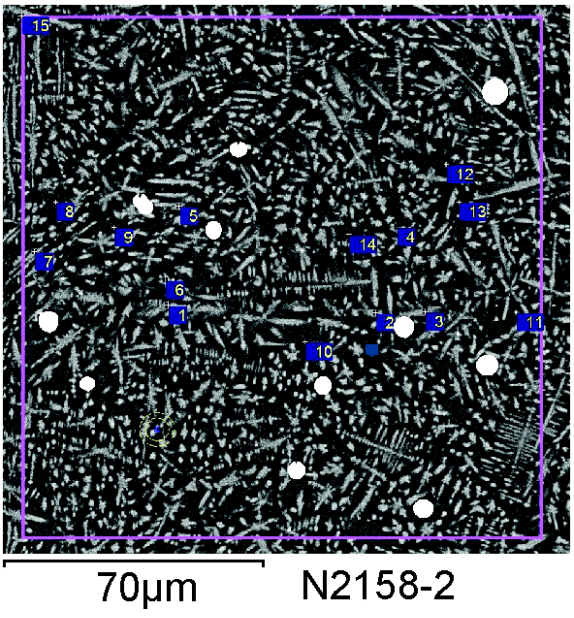

Fig. 1. Raster micrographs in reflected scattered electrons (BSE) of sample quenching products after experiments on crystallization of andesite melts under hydrogen pressure. Run No. 2158, repetition of experiment 2157, only the crystallization temperature is reduced to 900 °C, see the parameters of the experiment note to Table 1 (white color - Fe metal alloy, composition - see Tabl. 2, dark color - residual glass, light gray crystals: pyroxenes, plagioclases, composition - see Tabl. 1).

Under experimental conditions (1000 °C/10 MPa), the binary fluid (H_2O-H_2) is close to ideal, so that $f(i) = X(i) \cdot P$. Given that $X(H_2O) + X(H_2) = 1$ and $\Delta Go(1, 1373K)$ = -343.6 kJ (Barin, 1995), the solution of equation (1) leads to the value of $\log f(O_2)$ = -14.1, i.e. we have strongly reducing conditions in

the experiment, about an order of magnitude smaller than the iron-wustite buffer.

On the basis of experiments, the following features of the process of interaction of hydrogen with andesite melt were established. As previously established in the basalt-hydrogen system (Persikov et al., 2019), initially homogeneous andesite melts become heterogeneous and significantly more acidic compared to the original andesite (Tabl. 1). H_2O is formed in the fluid phase (initially pure hydrogen); H_2O (0.21 – 0.37 wt. %) dissolves in andesite melts, and small metal droplets of liquation texture are formed in them at a temperature of 1250 °C, well below the melting point of iron (1560 °C). The process of formation of a liquid-like structure of Fe (predominantly small spheres of several microns, (Fig. 1, the composition of the Tabl. 2) due to redox reactions, it is undoubtedly complex.

In crystallization experiments, it was found that the compositions of crystals (clinopyroxenes and plagioclases) formed in the experiment on crystallization of andesite melt closely correspond to the compositions of crystals of lava flows of the Avacha volcano in Kamchatka (Fig. 2). This result can be considered as an experimental confirmation of the participation of hydrogen in the magmatic process, which is also consistent with the composition of volcanic gases detected during the eruption of this volcano (Ivanov, 2008).

It should be noted that native iron of the liquation structure was not found in andesitic lava flows of Kamchatka volcanoes (Ivanov, 2008; Karpov and Mokhov, 2004) , which is apparently due to the higher viscosity of andesitic magmas compared to basaltic magmas. And, accordingly, with a slower rise from intermediate foci to the volcano, which ensured the oxidation of native iron. At the same time, native iron was often found in the ashes of andesitic volcanoes in Kamchatka (Karpov and Mokhov, 2004). An example of such native iron is shown in Fig. 3.

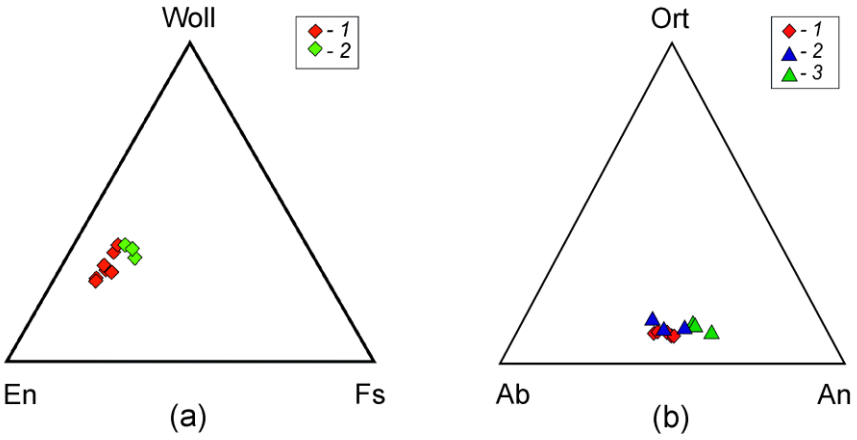

Fig. 2. Comparison of the composition of crystals formed in experiments No. 2157, 2158 with the compositions of natural minerals from lava flows of Avacha volcano, Kamchatka (Ivanov, 2008; green symbols). (a) - pyroxenes, experimental (red color): Wol = 29.94, En = 58.01, Fs = 12.05; natural: Wol = 34.2, En = 48.77, Fs = 17.03; (b) - plagioclase - experimental (red color - experiment 2157): An = 43.04, Ab = 47.39, Ort = 9.57; (blue color - experiment 2158): An = 42.71, Ab = 45.6, Ort= 11.69; natural: An = 52.49, Ab = 36.52, Ort = 10.99 .

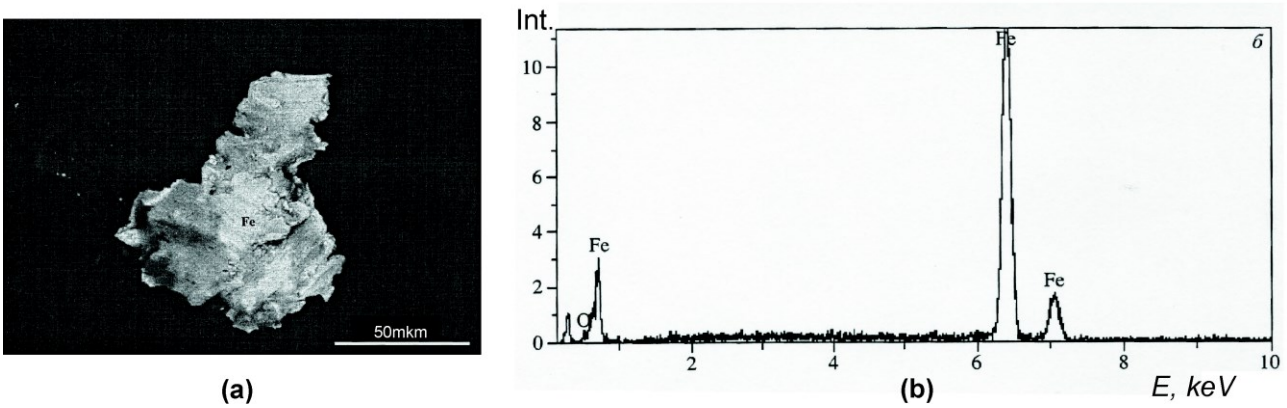

Fig. 3. A particle of metallic iron from the ashes. Sample 4437; a - is the image in scattered reflected electrons (BSE); b - is the energy dispersive X-ray spectrum from it (Karpov and Mokhov, 2004)

The work was carried out within the framework of the research topic No. FMUF-2022-0004 of the IEM RAS with the financial support of the Russian Science Foundation, grant No. 22-27-00124

References

Barin I. (1995) Thermochernical Data of Pure Substances. Third Edition. VCH Publishers, Inc., New York, USA, 1885 p.

Bird J.M., Goodrick C.A., Weathers M.S. (1981) Petrogenesis of Uiviaq iron, Disko Island, Greenland. *J. Geophys. Res.* B 86 (12), p. 11787-11806.

Ivanov, B.V. (2008) Andesites of Kamchatka, 470 p. (in Russian).

Levashov, V. K., Okrugin, B. V. (1984) Evaluation of the physical conditions for the formation of segregations of native iron in a basalt melt. Geochemistry and mineralogy of mafic, ultramafic rocks of the Siberian platform. Yakutsk, p. 54-62 (in Russian).

Marakushev A. A. (1995) Nature of native metals formation. Dokl. RAS, vol. 341, No. 6, 807-812.

Karpov, G.A., Mokhov, A.V. (2004) Accessory native ore minerals of eruptive ashes of andesite volcanoes of Kamchatka. Volcanology and Seismology, No. 4, p. 41-49 (in Russian).

Oleynikov, B.V., Okrugin, A.V., Tomshin, M.D., et al. (1985) Native metal formation in platform basites. (Edited by V.V. Kovalsky). Yakutsk: YaF SO AN SSSR, 124 p. (in Russian).

E.S. Persikov, P.G. Bukhtiyarov, L.Ya. Aranovich A.N., Nekrasov, O.Yu. Shaposhnikova (2019) Experimental modeling of formation of native metals (Fe,Ni,Co) in the earth's crust by the interaction of hydrogen with basaltic melts. Geohemistry International, Vol. 57, No. 10, p. 1035–1044.

Ryabov V. V., Pavlov A. L., Lopatin G. G. (1985) Native Iron in Siberian Traps. Novosibirsk: Nauka SB RAN, 167 p. (in Russian).

Shornikov S.I., Demidova S.I. Thermodynamic properties of the $CaO - P_4O_{10}$ melts.

V. I. Vernadsky Institute of Geochemistry & Analytical Chemistry RAS, Moscow sergey.shornikov@gmail.com

Abstract. The calculations of thermodynamic properties of the $CaO–P_4O_{10}$ melts in the temperature range 700–2100 K were carried out within the framework of the developed semi-empirical model. The calculated values of partial pressures of vapor species, as well as the oxide activities and the mixing energies in the melts are compared with the available information.

Keywords: thermodynamic properties of oxide melts, evaporation, the $CaO–P_4O_{10}$ system

Phosphorus is an important minor element of the lunar rocks. It has moderate volatility and is usually present as phosphates (merrilite, apatite). Considerable interest in them is caused by the discovery of the OH−bearing apatites in a number of mare basalts, that contradicts the early statement about dryness of the lunar basaltic magmas. To clarify the conditions of the crystallization of phosphates from the melt, theoretical calculations of the thermodynamic properties of the $CaO–P_4O_{10}$ melts at high temperatures were carried out.

The presence of eight calcium phosphates in the $CaO–P_4O_{10}$ system has been established. They exist in various structural modifications depending on temperature. The $Ca_3P_2O_8$ ($6CaO \cdot P_4O_{10}$), $Ca_2P_2O_7$ ($4CaO \cdot P_4O_{10}$), CaP_2O_6 ($2CaO \cdot P_4O_{10}$) and CaP_4O_{11} ($CaO \cdot P_4O_{10}$) compounds melt congruently at 2076, 1622, 1251 and 1046 K, respectively. The $Ca_4P_2O_9$ ($8CaO \cdot P_4O_{10}$), $Ca_4P_6O_{19}$ ($8CaO \cdot 3P_4O_{10}$) and $Ca_2P_6O_{17}$ ($4CaO \cdot 3P_4O_{10}$) compounds dissociate at 2021, 1242 and 1040 K, respectively. The $Ca_{10}P_6O_{25}$ ($20CaO \cdot 3P_4O_{10}$) calcium phosphate exists in a limited temperature range of 1126–1323 K. It decomposes into α-$Ca_4P_2O_9$ and β-$Ca_3P_2O_8$. The phase diagram of the $CaO–P_4O_{10}$ system according to the survey data (Hudon, Jung, 2015) is shown in Fig. 1.

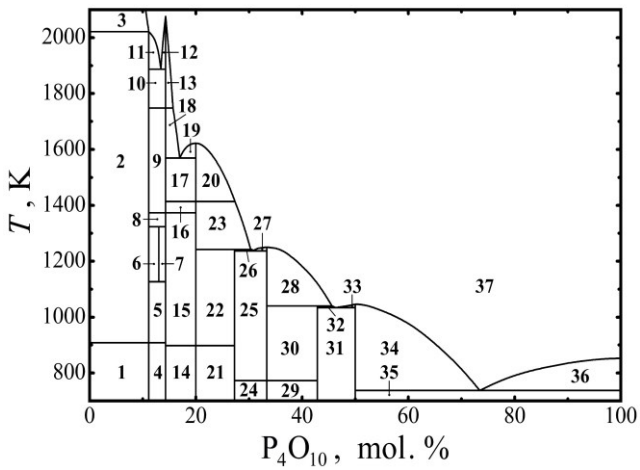

Fig. 1. The phase diagram of the $CaO–P_4O_{10}$ system (Hudon, Jung, 2015).

List of symbols: 1 – CaO + β-$Ca_4P_2O_9$; 2 – CaO + α-$Ca_4P_2O_9$; 3 – CaO + liquid; 4 – β-$Ca_4P_2O_9$ + β-$Ca_3P_2O_8$; 5 – α-$Ca_4P_2O_9$ + β-$Ca_3P_2O_8$; 6 – α-$Ca_4P_2O_9$ + $Ca_{10}P_6O_{25}$; 7 – $Ca_{10}P_6O_{25}$ + β-$Ca_3P_2O_8$; 8 – α-$Ca_4P_2O_9$ + β-$Ca_3P_2O_8$; 9 – α-$Ca_4P_2O_9$ + α-$Ca_3P_2O_8$; 10 – α-$Ca_4P_2O_9$ + α'-$Ca_3P_2O_8$; 11 – α-$Ca_4P_2O_9$ + liquid; 12, 13 – α'-$Ca_3P_2O_8$ + liquid; 14 – β-$Ca_3P_2O_8$ + γ-$Ca_2P_2O_7$; 15 – β-$Ca_3P_2O_8$ + β-$Ca_2P_2O_7$; 16 – α-$Ca_3P_2O_8$ + β-$Ca_2P_2O_7$; 17 – α-$Ca_3P_2O_8$ + α-$Ca_2P_2O_7$; 18 – α-$Ca_2P_2O_7$ + liquid; 19, 20 – α-$Ca_2P_2O_7$ + liquid; 21 – γ-$Ca_2P_2O_7$ + $Ca_4P_6O_{19}$; 22 – β-$Ca_2P_2O_7$ + $Ca_4P_6O_{19}$; 23 – β-$Ca_2P_2O_7$ + liquid; 24 – $Ca_4P_6O_{19}$ + γ-CaP_2O_6; 25 – $Ca_4P_6O_{19}$ + β-CaP_2O_6; 26 – $Ca_4P_6O_{19}$ + liquid; 27, 28 – α-CaP_2O_6 + liquid; 29 – γ-CaP_2O_6 + $Ca_2P_6O_{17}$; 30 – β-CaP_2O_6 + $Ca_2P_6O_{17}$; 31 – $Ca_2P_6O_{17}$ + α-CaP_4O_{11}; 32 – $Ca_2P_6O_{17}$ + liquid; 33, 34 – α-CaP_4O_{11} + liquid; 35 – α-CaP_4O_{11} + P_4O_{10}; 36 – P_4O_{10} + liquid; 37 – liquid.

The available thermodynamic data on calcium phosphates are quite contradictory: errors in determining the values of the enthalpy of compound formation exceed 10 kJ/mol, and in the values of the entropy of formation – at least 5 J/(mol×K). Measurements of CaO activity in the $CaO–P_4O_{10}$ melt were performed in a narrow concentration range (11–22 mol % P_4O_{10}) at 1923 K in a single experimental study (Schwerdtfeger, Engell, 1963) (Fig. 2). The partial pressures of (PO), (PO_2) and (P_4O_{10}) vapor species over congruently melting calcium phosphates (Butylin et al., 1975; Ratkovsky et al., 1975; Lopatin, Semenov, 1989; Lopatin, 1997) and mixtures of calcium phosphates with alloys (Nagai et al.., 2009) were determined by the Knudsen effusion mass spectrometry method in a wide temperature range of 800–1900 K (Fig. 3). The ($CaPO_2$) vapor specie deficient in oxygen was detected in the gas phase over $Ca_3P_2O_8$ at 2046 K (Lopatin, Semenov, 1986). Evaporation of calcium phosphates was carried out from platinum (Ratkovsky et al., 1975), molybdenum (Lopatin, Semenov, 1986; Lopatin, Semenov, 1989; Nagai et al., 2009) and alund (Butylin et al., 1975; Ratkovsky et al., 1975) effusion cells. The use of the latter can lead to chemical interaction with phosphate samples (Lopatin, 1997) and, thereby, distort the measurement results. Based on the data of Lopatin and Semenov (1989), it was possible to estimate the P_4O_{10} activity in the $Ca_3P_2O_8$ compound at 1900 K, equal to 2.21×10^{-38} (Fig. 2). A detailed review of the available physicochemical data and an assessment of thermodynamic properties in the $CaO–P_4O_{10}$ system was recently carried out in (Jantzen et al., 2019).

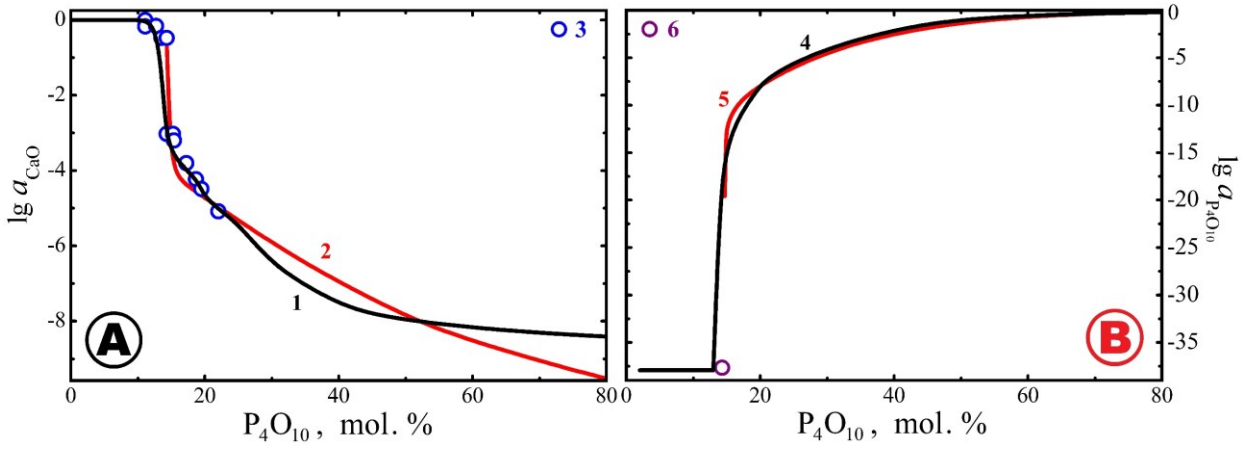

Fig. 2. The activities of CaO (1–3) (A) and P4O10 (4–6) (B) in the CaO–P4O10 melts at 1900 (6) and 1923 (1–5) K calculated at the present study (1, 4) and in (Hudon, Jung, 2015) (2, 5), and also determined experimentally in (Schwerdtfeger, Engell, 1963) (3) and (Lopatin, Semenov, 1989) (6).

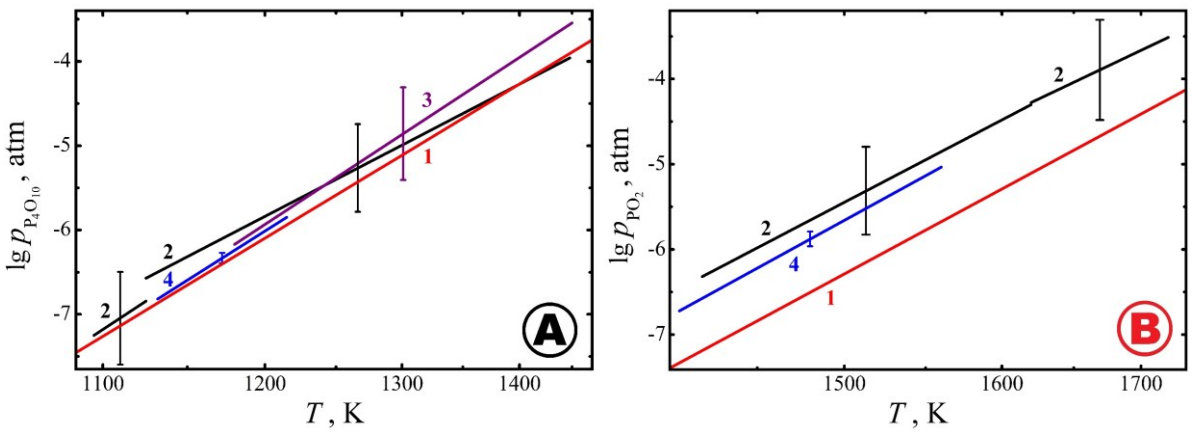

Fig. 3. The temperature dependence of partial pressures of (P_4O_{10}) over CaP_2O_6 (A) and (PO_2) over $Ca_2P_2O_7$ (B) calculated at the present study (1) and determined by the Knudsen effusion mass spectrometric method in (Butylin et al., 1975) (2), (Ratkovsky et al., 1975) (3) and (Lopatin, 1997) (4).

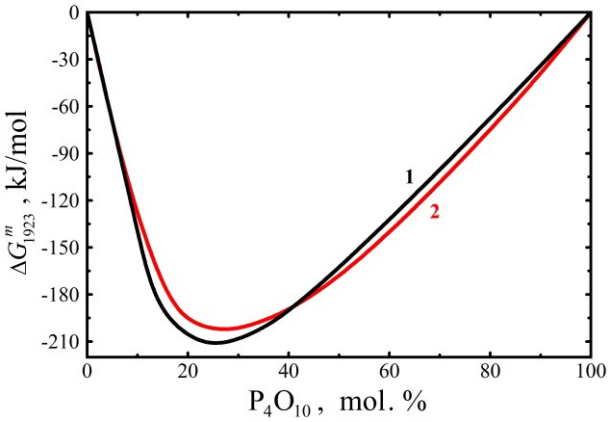

Fig. 4. The mixing energies in the $CaO–P_4O_{10}$ melts at 1923 K, calculated at the present study (1) and in (Hudon, Jung, 2015) (2).

The theoretical calculations of thermodynamic properties of the $CaO–P_4O_{10}$ melts in the temperature range 700–2100 K were performed using a semi-empirical model (Shornikov, 2019) in order to clarify its parameters. The model parameters were the values of the Gibbs energies ($\Delta G°$) calculated from experimental and theoretical data for the formation of simple oxides (CaO and P_4O_{10}) and calcium phosphates (CaP_4O_{11}, $Ca_2P_6O_{17}$, CaP_2O_6, $Ca_4P_6O_{19}$, $Ca_2P_2O_7$, $Ca_3P_2O_8$, $Ca_{10}P_6O_{25}$ and $Ca_4P_2O_9$). The initial values of the Gibbs energies of formation of CaO and P_4O_{10} in the crystalline and liquid state, as well as information on possible equilibria in the gas phase over the melt involving atomic and molecular vapor species (Ca, Ca_2, CaO, P, P_2, P_3, P_4, PO, PO_2, P_2O_3, P_2O_4, P_2O_5, P_3O_6, P_4O_6, P_4O_7, P_4O_8, P_4O_9, P_4O_{10}, O, O_2, O_3 and O_4) were adopted on the reference data (Glushko et al., 1978–1982). The $\Delta G°$ values of condensed phases and vapor species over the melt were used to find equilibrium conditions for a given melt composition and temperature.

A comparison of the results of calculations of the oxide activities (a_i) (Fig. 2) and the mixing energies (ΔG^m) (Fig. 4) in the $CaO–P_4O_{10}$ melts at 1923 K obtained at the present study with those obtained by Hadon and Zhang (2015), as well as with experimental data obtained in (Schwerdtferger, Engell, 1963; Lopatin, Semenov, 1989), shows their satisfactory correspondence. The calculated oxide activities in the the $CaO–P_4O_{10}$ melt correspond to the position of the liquid phase in the phase diagram of the system (Fig. 1). The minimum value of the mixing energy in the $CaO–P_4O_{10}$ melts is in the composition region close to $Ca_2P_2O_7$ and is equal to –210 kJ/mol.

As follows from Fig. 3A, the calculated partial pressures of (P_4O_{10}) gaseous phosphorus oxide over CaP_2O_6 calcium phosphate correspond satisfactorily to the experimental data obtained by the Knudsen effusion mass spectrometric method in (Butylin et al., 1975; Ratkovsky et al., 1975; Lopatin, 1997). The higher partial pressure values of (PO_2) gaseous oxide over $Ca_2P_2O_7$ obtained by Lopatin (1997) are due to the presence of reducing conditions occurring in the case of a molybdenum effusion cell (Fig. 3B). The observed difference between the calculated values of (PO_2) partial pressure and the results obtained by Butylin et al. (1975) illustrates the above-mentioned interaction of the phosphate melt with the alund effusion cell which they used in the experiments (Fig. 3B).

References

Butylin B. A., Ratkovsky I. A., Ershov V. A., Novikov G. I. (1975) Thermodynamic study of the processes of thermal dissociation of calcium meta-, pyro- and orthophosphates // *Doklady AN BSSR*, vol. 19, no. 7, pp. 618–621.

Glushko V. P., Gurvich L. V., Bergman G. A., Veitz I. V., Medvedev V. A., Khachkuruzov G. A., Yungman V. S. (1978–1982) Thermodynamic properties of individual substances. Moscow: Nauka.

Hudon P., Jung I.-H. (2015) Critical evaluation and thermodynamic optimization of the $CaO–P_2O_5$ system. *Met. Mater. Trans*. B, vol. 46, no. 1, pp. 494–522.

Jantzen T., Yazhenskikh E., Hack K., Muller M. (2019) Thermodynamic assessment of the $CaO–P_2O_5–SiO_2–ZnO$ system with special emphasis on the addition of ZnO to the $Ca_2SiO_4–Ca_3P_2O_8$ phase. *CALPHAD*, vol. 67, no. 101668.

Lopatin S. I., Semenov G. A. (1986) Gaseous phosphates of calcium, strontium and barium. *Doklady AN SSSR*, vol. 287, no. 2, pp. 380–381.

Lopatin S. I., Semenov G. A. (1989) Mass spectrometric investigation of thermal dissociation of alkaline earth metal monophosphates. *Izv. AN SSSR. Neorg. Mater*., vol. 25, no. 4, pp. 645–650.

Lopatin S. I. (1997) Vaporization in phosphate systems. *Russ. J. Gen. Chem*., vol. 67, no. 2, pp. 208–227.

Nagai T., Miyake M., Maeda M. (2009) Thermodynamic measurement of calcium phosphates by double Knudsen cell mass spectrometry. *Met. Mater. Trans. B*, vol. 40, no. 4, pp. 544–549.

Ratkovsky I. A., Butylin B. A., Novikov G. I. (1975) Thermodynamic investigation of the process of thermal dissociation of $Ca(PO_3)_2$. *Doklady AN BSSR*, vol. 19, no. 2, pp. 139–140.

Schwerdtfeger K., Engell H. J. Die aktivitaten im system kalziumoxyd–phosphorsaure bei 1650 °C // Arch. Eisenhuettenwes. 1963. V. 34. № 9. P. 647–652.

Shornikov S. I. (2019) Thermodynamic modelling of evaporation processes of lunar and meteoritic substance. *Geochem. Int*., vol. 57, no. 8, pp. 865–872.

Shornikov S.I.[1], Slobodov A.A.[2] Thermodynamic properties of the $SiO_2–P_4O_{10}$ melts

[1]V. I. Vernadsky Institute of Geochemistry & Analytical Chemistry RAS, Moscow (sergey.shornikov@gmail.com)

[2] Saint-Petersburg State Institute of Technology, St. Petersburg

Abstract. Within the framework of the developed semi-empirical model, the thermodynamic properties of the SiO_2–P_4O_{10} melts were calculated in the temperature region 700–2000 K. The calculated values of the oxide activities and the mixing energies in the melts are compared with the available information.

Keywords: thermodynamic properties of oxide melts, evaporation, the SiO_2–P_4O_{10} system

The physicochemical properties of the SiO_2–P_4O_{10} system are of considerable interest for understanding the formation of phosphorus-containing olivine in lunar meteorites, as well as for practical application in fiber optics. The existence of the SiP_2O_7 and $Si_3(PO_4)_4$ silicon phosphates has been established in the SiO_2–P_4O_{10} system (Makart, 1967). The SiP_2O_7 ($2SiO_2 \cdot P_4O_{10}$) compound exists in hexagonal (*H*), two monoclinic (*M*), tetragonal (*T*) and cubic (*C*) modifications with the transition temperatures of *M*-SiP_2O_7 and *T*-SiP_2O_7 equal to 1380 K and 1480 K, respectively, and the last modification – *C*-SiP_2O_7 melts congruently at 1561 K (Baret et al., 1991). The $Si_3(PO_4)_4$ ($3SiO_2 \cdot P_4O_{10}$) trisilicon phosphate dissociates at 1392 K into *T*-SiP_2O_7 and liquid (Jantzen et al., 2019). Malshikov and Bondar (1988) believe that this compound has the composition of $Si_5O(PO_4)_6$ ($10SiO_2 \cdot 3P_4O_{10}$) and decomposes into *C*-SiP_2O_7 and liquid. One of the variants of the phase diagram of the SiO_2–P_4O_{10} system according to the reviews (Rahman et al., 2013; Jantzen et al., 2019) is shown in Fig.1. Thermodynamic information on the compounds of the SiO_2–P_4O_{10} system is not numerous. Baret et al. (1991) determined the enthalpy of transitions of SiP_2O_7 and $Si_3(PO_4)_4$ by the DTA method. Flemish and Tressler (1991) determined the total vapor pressure over the SiP_2O_7 by the transpiration method at 1198–1298 K. Lopatin and Semenov (1995) studied the SiP_2O_7 evaporation from a molybdenum effusion cell by mass spectrometry and determined the partial pressures of the (PO) predominant vapor specie at 1400–1484 K. No other molecules were detected in addition to the (PO), (PO_2) and (SiO) vapor species. The thermodynamic properties of compounds and melts were evaluated in (Rahman et al., 2013; Jantzen et al., 2019) based on the available physicochemical data on the SiO_2–P_4O_{10} system.

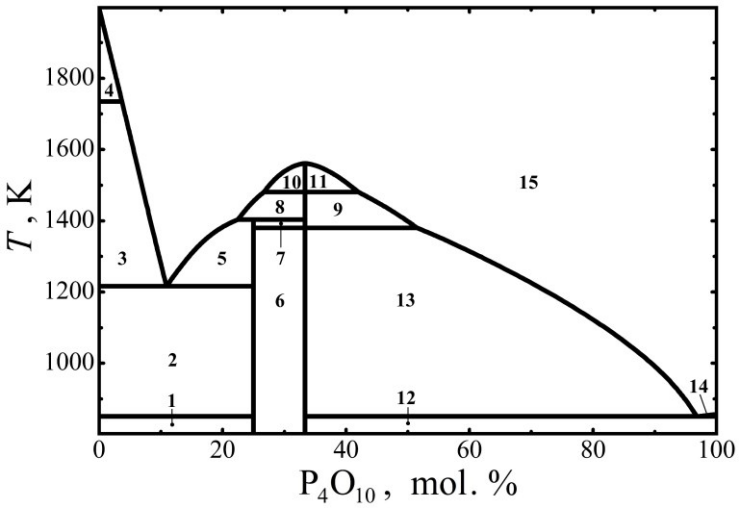

List of symbols:
1 – α-SiO_2 (quartz) + $Si_3P_4O_{16}$; 2 – β-SiO_2 (quartz) + $Si_3P_4O_{16}$; 3 – β-SiO_2 (tridymite) + liquid; 4 – β-SiO_2 (cristobalite) + liquid; 5 – $Si_3P_4O_{16}$ + liquid; 6 – $Si_3P_4O_{16}$ + *M*-SiP_2O_7; 7 – $Si_3P_4O_{16}$ + *T*-SiP_2O_7; 8, 9 – *T*-SiP_2O_7 + liquid; 10, 11 – *C*-SiP_2O_7 + liquid; 12 – *M*-SiP_2O_7 + P_4O_{10}; 13 – *M*-SiP_2O_7 + liquid; 14 – P_4O_{10} + liquid; 15 – liquid.

Fig. 1. The phase diagram of the SiO_2–P_4O_{10} system (Rahman et al., 2013; Jantzen et al., 2019).

The theoretical calculations of the thermodynamic properties of the SiO_2–P_4O_{10} melts were performed at the present study at 700–2000 K using a semi-empirical model (Shornikov, 2019) in order to clarify its parameters. The model parameters were the values of the Gibbs energies ($\Delta G°$) calculated from experimental and theoretical data for the formation of simple oxides (SiO_2 and P_4O_{10}) and silicon phosphates (SiP_2O_7 and $Si_3P_4O_{16}$). The initial values of the Gibbs energies of SiO_2 and P_4O_{10} formation in the crystalline and liquid state, as well as information on possible equilibria in the gas phase over the melt involving atomic and molecular species (Si, Si_2, Si_3, SiO, SiO_2, Si_2O_2, P, P_2, P_3, P_4, PO, PO_2, P_2O_3, P_2O_4, P_2O_5, P_3O_6, P_4O_6, P_4O_7, P_4O_8, P_4O_9, P_4O_{10}, O, O_2, O_3 and O_4) were adopted based on reference data (Glushko et al., 1978–1982). The $\Delta G°$ values of condensed phases and vapor species over the melt were used to find equilibrium conditions at a given melt composition and temperature.

The calculated oxide activities (a_i) and mixing energies (ΔG^m) in the SiO_2–P_4O_{10} melts compare with the results obtained in (Rahman et al., 2013) in Fig. 2 and 3.

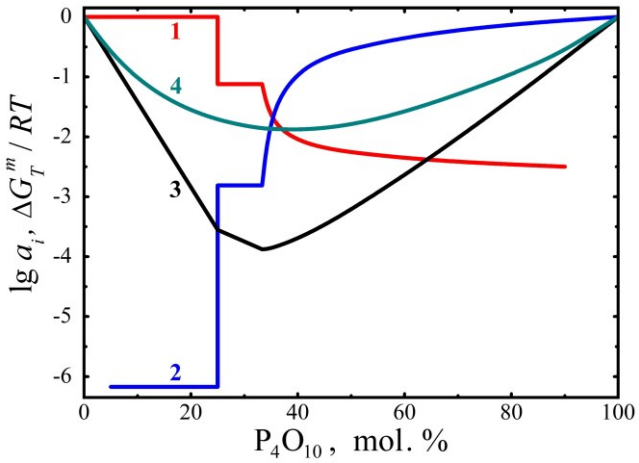

Fig. 2. The SiO_2 (1) and P_4O_{10} (2) activities and mixing energies (3, 4) in the SiO_2–P_4O_{10} melts at 1100 (1–3) and 1873 (4) K, calculated at the present study (1–3) and in (Rahman et al., 2013) (4).

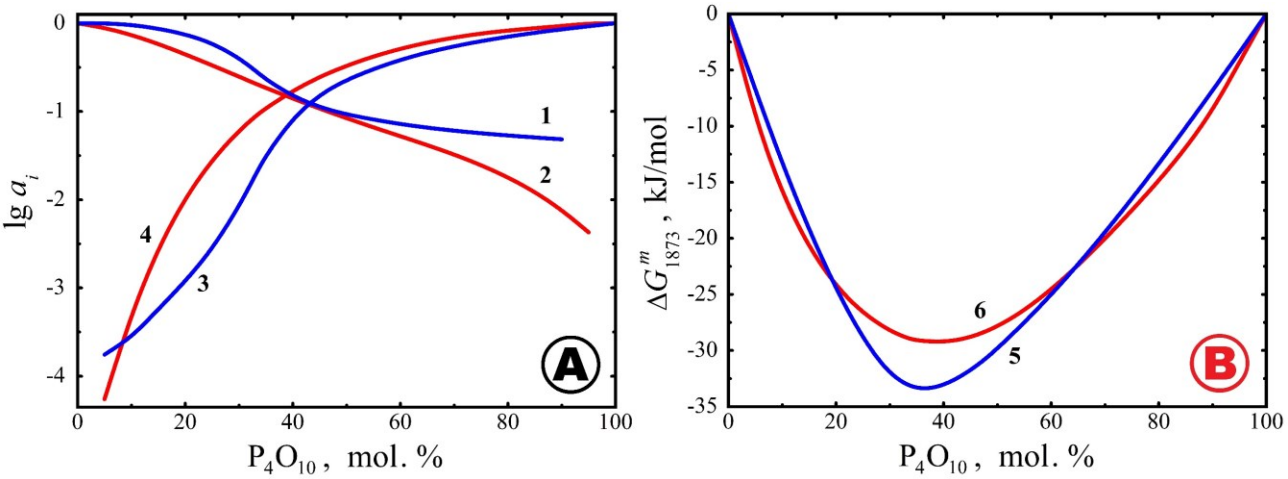

Fig. 3. The activities of SiO_2 (1, 2) and P_4O_{10} (3, 4) (A) and the mixing energies (5, 6) (B) in the SiO_2–P_4O_{10} melts at 1873 K, calculated at the present study (1, 3, 5) and in (Rahman et al., 2013) (2, 4, 6).

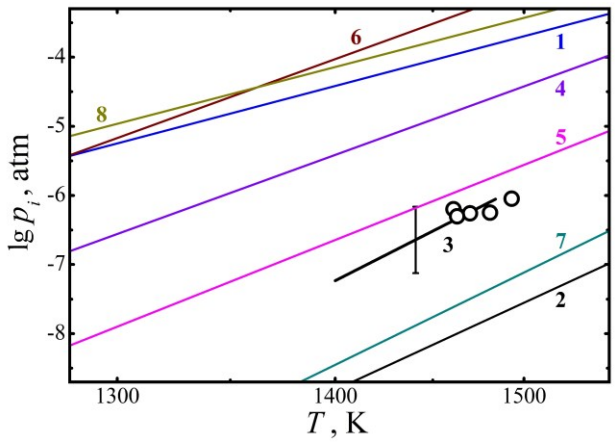

Fig. 4. The temperature dependencies of partial pressures of O_2 (1), PO (2, 3), PO_2 (4), P_2O_3 (5), P_2O_4 (6), P_2O_5 (7) and P_4O_9 (8) over the SiP_2O_7 calculated at the present study (1, 2, 4–8) and determined by the Knudsen effusion mass spectrometric method (Lopatin, Semenov, 1995) (3).

As follows from Fig. 2, the SiO_2 and P_4O_{10} activities at 1100 K show a sharp change during the transition from the "β-SiO_2 + $Si_3P_4O_{16}$" phase region to the "$Si_3P_4O_{16}$ + *M*-SiP_2O_7" phase region, which corresponds to the phase diagram of the SiO_2–P_4O_{10} system (Fig. 1, regions 2 and 6). In this case, the minimum mixing energy value for the SiP_2O_7 composition is reached, equal to –35 kJ/mol. With an increase in temperature, the position of the minimum mixing energy in the melt is maintained with an increase in the ΔG^m value to –33 kJ/mol at 1873 K (Fig. 3).

Figure 4 shows the temperature dependencies of the partial pressures of vapor species over SiP_2O_7, calculated at the present study and experimentally determined by the Knudsen effusion mass

spectrometric method (Lopatin, Semenov, 1995). The higher values of the (PO) partial pressures obtained by Lopatin and Semenov (1995) are due to the presence of reducing conditions caused by the interaction of the molybdenum effusion cell with the melt contained therein.

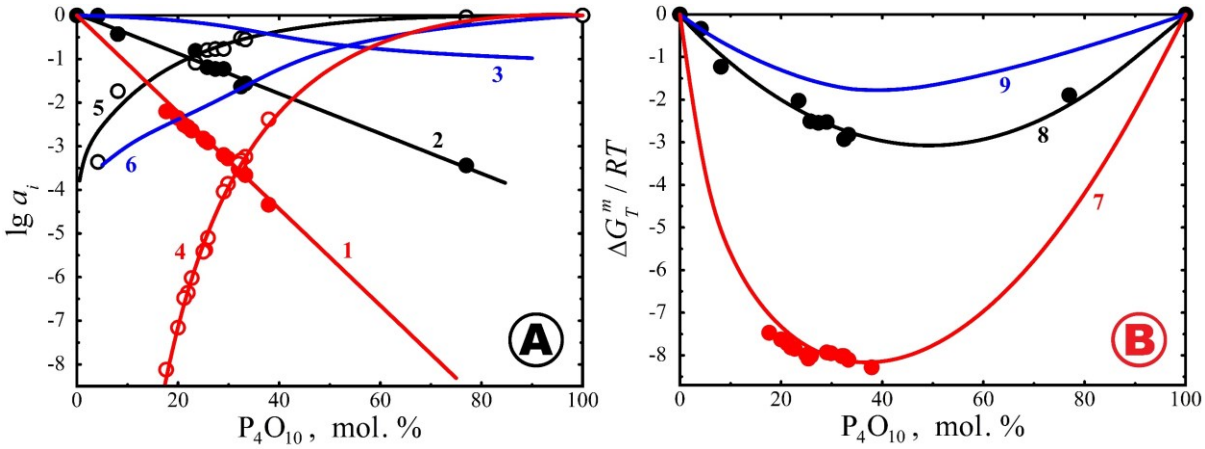

Fig. 5. The ZnO (1), GeO_2 (2), SiO_2 (3) and P_4O_{10} (4–6) activities (A) and the mixing energies (7–9) (B) in the ZnO–P4O10 melts at 1300 K (1, 4, 7), in the GeO_2–P_4O_{10} melts at 1423 K (2, 5, 8) and in the SiO_2–P_4O_{10} melts at 2000 K (3, 6, 9), determined in (Shornikov et al., 1996; Stolyarova et al., 1990) and calculated at the present study, respectively.

A comparison of oxide activities and mixing energies in the phosphate silicate melts (Fig. 5) with those for the ZnO–P_4O_{10} (Shornikov et al., 1996) and the GeO_2–P_4O_{10} (Stolyarova et al., 1990) studied phosphate melts shows the smallest chemical interaction in the SiO_2–P_4O_{10} melts, characteristic of this series of phosphate melts.

References

Baret G., Madar R., Berbard C. (1991) Silica-based oxide systems. I. Experimental and calculated phase equilibria in silicon, boron, phosphorus, germanium, and arsenic oxide mixtures. *J. Electrochem. Soc*., vol. 138, no. 9, pp. 2830–2835.

Flemish J. R., Tressler R. (1991) P_xO_y evaporation from SiP_2O_7 and its relationship to phosphosilicate glass films. *J. Electrochem. Soc*., vol. 138, no. 12, pp. 3743–3747.

Glushko V. P., Gurvich L. V., Bergman G. A., Veitz I. V., Medvedev V. A., Khachkuruzov G. A., Yungman V. S. (1978–1982) Thermodynamic properties of individual substances. Moscow: Nauka.

Jantzen T., Yazhenskikh E., Hack K., Muller M. (2019) Thermodynamic assessment of the CaO–P_2O_5–SiO_2–ZnO system with special emphasis on the addition of ZnO to the Ca_2SiO_4–$Ca_3P_2O_8$ phase. *CALPHAD*, vol. 67, no. 101668.

Lopatin S. I., Semenov G. A. (1995) Vaporization processes of silicon and germanium diphosphates. Russ. *J. Gen. Chem*., vol. 65, no. 7, pp. 1060-1064.

Makart H. (1967) Untersuchungen an siliciumphosphaten. *Helv. Chim. Acta*, vol. 50, no. 47, pp. 399–405.

Malshikov A. E., Bondar I. A. (1988) Physico-chemical investigation of the SiO_2–P_2O_5 system. Russ. J. *Neorgan. Chem.,* vol. 33, no. 1, pp. 198–202.

Rahman M., Hudon P., Jung I.-H. (2013) A coupled experimental study and thermodynamic modeling of the SiO_2–P_2O_5 system. *Met. Mater. Trans. B*, vol. 44, no. 8, pp. 837–852.

Shornikov S. I., Shilov A. L., Shultz M. M. (1996) A mass-spectrometric study of the thermodynamic properties of ZnO–P_2O_5 system melts. *Russ. J. Phys. Chem*., vol. 70, no. 3, pp. 447–453.

Shornikov S. I. (2019) Thermodynamic modelling of evaporation processes of lunar and meteoritic substance. *Geochem. Int*., vol. 57, no. 8, pp. 865–872.

Stolyarova V. L., Shornikov S. I., Ivanov G. G., Shultz M. M. (1990) Mass spectrometric study of vaporization processes and thermodynamic properties in the GeO_2–P_2O_5 system. *Rapid Commun. Mass Spectr*., vol. 4, no. 12, pp. 510–512.

Shornikov S.I.[1], Golyapa E.S.[2] Thermodynamic properties of the MgO–P_4O_{10} melts.

[1]V. I. Vernadsky Institute of Geochemistry & Analytical Chemistry RAS, Moscow sergey.shornikov@gmail.com

[2]*WORKME Ltd, Saint-Petersburg*

Abstract. Within the framework of the developed semi-empirical model, the thermodynamic properties of the MgO–P_4O_{10} melts were calculated in the temperature range of 600–1800 K. The calculated values of the partial pressures of vapor species as well as the oxide activities and the mixing energies in the melts are compared with available information.

Keywords: thermodynamic properties of oxide melts, evaporation, the MgO–P_4O_{10} system

The formation of phosphorus-containing olivines found in lunar matter is of considerable interest for

the Moon geochemistry (Demidova et al., 2019). In order to understand the conditions of olivine formation and crystallization at high temperatures, calculations of the thermodynamic properties of the $MgO–P_4O_{10}$ melts are performed at the present study.

It has been found four magnesium phosphates in the $MgO–P_4O_{10}$ system – $Mg_3P_2O_8$ ($6MgO \cdot P_4O_{10}$), $Mg_2P_2O_7$ ($4MgO \cdot P_4O_{10}$), MgP_2O_6 ($2MgO \cdot P_4O_{10}$) and MgP_4O_{11} ($MgO \cdot P_4O_{10}$). They melt congruently at 1630, 1658, 1438 and 1183 K, respectively (Berak, 1958). The $Mg_3P_2O_8$ compound exists in two polymorphic forms with a transition temperature equal to 1328 K. A variant of the phase relation in the $MgO–P_4O_{10}$ system according to the survey data (Ding et al., 2015) is shown in Fig. 1.

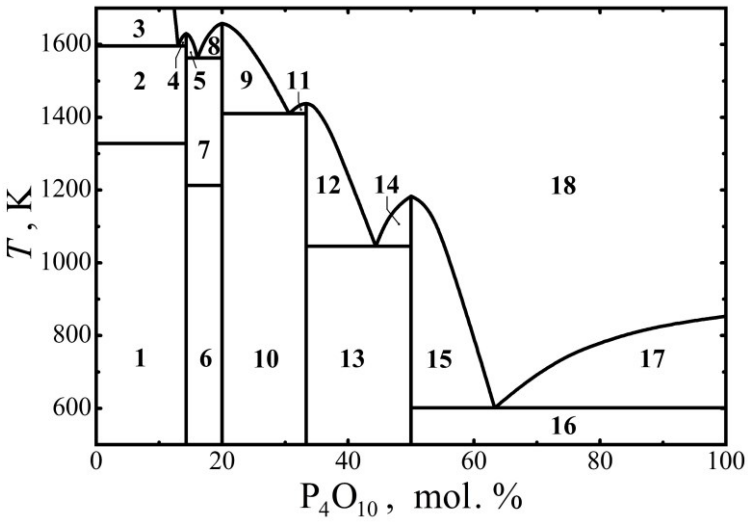

List of symbols:
1 – MgO + β-$Mg_3P_2O_8$; 2 – MgO + α-$Mg_3P_2O_8$; 3 – MgO + liquid; 4, 5 – α-$Mg_3P_2O_8$ + liquid; 6 – β-$Mg_3P_2O_8$ + $Mg_2P_2O_7$; 7 – α-$Mg_3P_2O_8$ + $Mg_2P_2O_7$; 8, 9 – $Mg_2P_2O_7$ + liquid; 10 – $Mg_2P_2O_7$ + MgP_2O_6; 11, 12 – MgP_2O_6 + liquid; 13 – MgP_2O_6 + MgP_4O_{11}; 14, 15 – MgP_4O_{11} + liquid; 16 – MgP_4O_{11} + P_4O_{10}; 17 – P_4O_{10} + liquid; 18 – liquid.

Fig. 1. The phase diagram of the $MgO–P_4O_{10}$ system (Ding et al., 2015).

The few data on the thermodynamic properties on compounds and melts in the $MgO–P_4O_{10}$ system are reviewed in (Jung et al., 2013; Ding et al., 2015). The heat capacities and enthalpy of melting of $Mg_3P_2O_8$ and $Mg_2P_2O_7$ were determined in (Oetting, McDonald, 1963). The phosphorus oxide activity was determined by the EMF method at 1673 K in a single study (Iwase et al., 1987) in a narrow concentration range (8–14 mol. % P_4O_{10}). The evaporation of magnesium phosphates of $Mg_3P_2O_8$, $Mg_2P_2O_7$ and MgP_2O_6 from platinum and molybdenum effusion cells was studied by mass spectrometry (Lopatin et al., 1986; Lopatin, Semenov, 1989; Lopatin, Shugurov, 2005). The temperature dependencies of the partial pressures of vapor species of (P_4O_{10}) over MgP_2O_6 (1263–1388 K), (PO_2) over $Mg_2P_2O_7$ (1416–1524 K), as well as (PO) and (Mg) over $Mg_3P_2O_8$ (1695–1810 K) were determined. The ($MgPO_2$) and ($MgPO_3$) gaseous oxides deficient on oxygen were found in the gas phase over the mixtures of magnesium oxide and magnesium phosphates at 1680–2009 K (Lopatin, Shugurov, 2005).

The values of oxide activities (a_i) and mixing energies (ΔG^m) in the $MgO–P_4O_{10}$ melts were calculated at the present study at 600–1800 K. The used semi-empirical model was described in detail earlier (Shornikov, 2019). The initial data were information of Glushko et al. (1978–1982) on the Gibbs energies ($\Delta G°$) of formation of simple oxides (MgO and P_4O_{10}), as well as data of Jung et al. (2013) and Ding et al. (2015) for calculations of $\Delta G°$ of magnesium phosphates ($Mg_3P_2O_8$, $Mg_2P_2O_7$, MgP_2O_6 and MgP_4O_{11}) in the crystalline and liquid phases. Calculations took into account the presence of the following vapor species in the gas phase over the melt: Mg, Mg_2, MgO, P, P_2, P_3, P_4, PO, PO_2, P_2O_3, P_2O_4, P_2O_5, P_3O_6, P_4O_6, P_4O_7, P_4O_8, P_4O_9, P_4O_{10}, $MgPO_2$, $MgPO_3$, O, O_2, O_3 and O_4. The $\Delta G°$ values of condensed phases and the gas phase species over the melt were used to find equilibrium conditions for a given melt composition and temperature.

A comparison of the results of calculating oxide activities and mixing energies in the $MgO–P_4O_{10}$ melts obtained at the present study (Fig. 2) at 1400–1800 K with those obtained by Ding et al. (2015), as well as with experimental information obtained in (Iwase et al., 1987; Lopatin et al., 1986; Lopatin, Semenov, 1989) shows their satisfactory correspondence. The calculated oxide activities in the $MgO–P_4O_{10}$ melts correspond to the position of the liquid phase in the phase diagram of the system (Fig. 1). The minimum value of mixing energy in the $MgO–P_4O_{10}$ melts at 1673 K is in the composition region close to MgP_2O_6 and is equal to –175 kJ/mol.

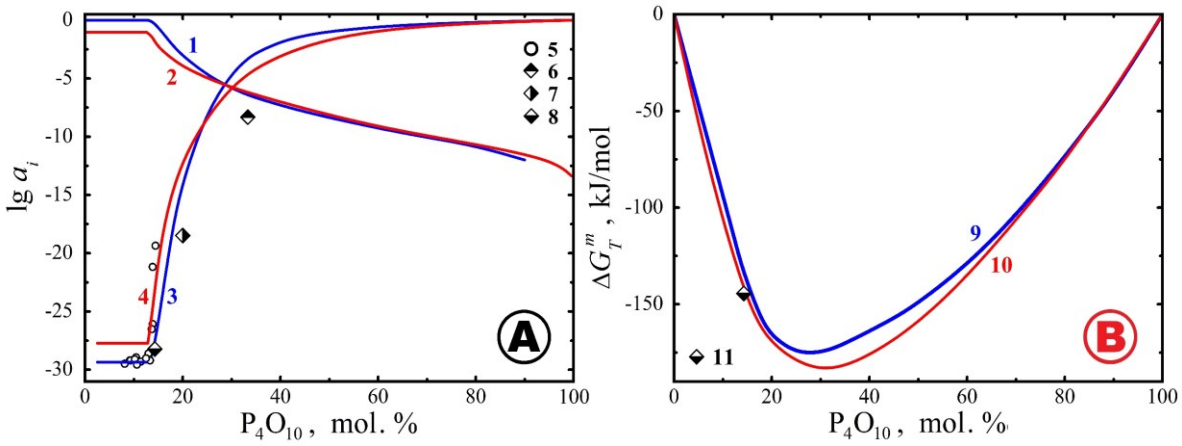

Fig. 2. The activity of MgO (1, 2) and P_4O_{10} (3–8) (A), as well as the mixing energy (9–11) (B) in the MgO– P_4O_{10} melts at 1400 (6), 1600 (7), 1673 (1–5, 9, 10) and 1800 (8, 11) K calculated at the present study (1, 3, 9) and in (Ding et al., 2015) (2, 4, 10), and dedermined experimentally in (Oetting, McDonald, 1963) (5), (Lopatin et al., 1986) (6, 7) and (Lopatin, Semenov, 1989) (8, 11).

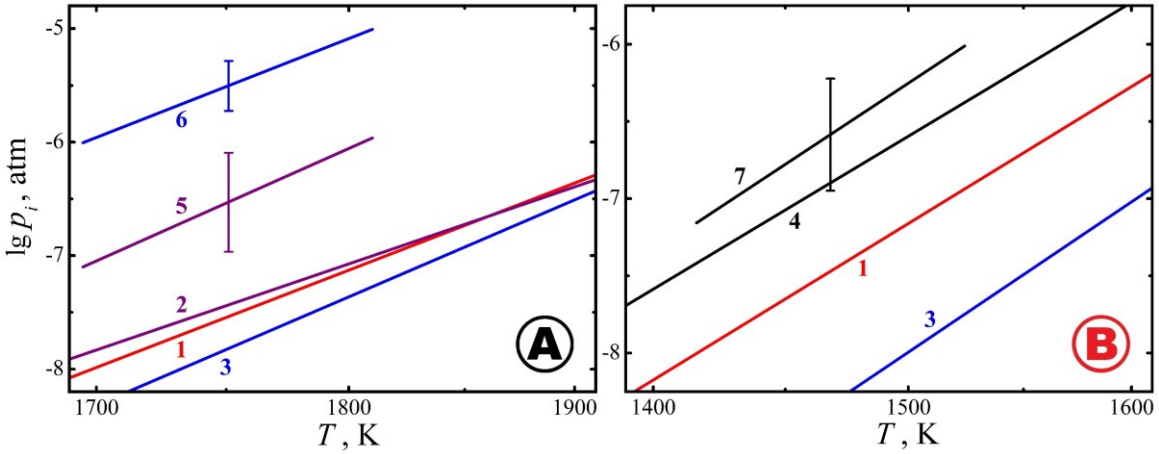

Fig. 3. The temperature dependencies of partial pressures of (O_2) (1), (Mg) (2, 5), (PO) (3, 6) and (PO_2) (4, 7) vapor species over $Mg_3P_2O_8$ (A) and $Mg_2P_2O_7$ (B) calculated at the present study (1–4) and determined by the Knudsen effusion mass spectrometric method in (Lopatin, Semenov, 1989) (5, 6) and (Lopatin et al., 1986) (7).

As follows from Fig. 3, the calculated partial pressures of (Mg), (PO) and (PO_2) vapor species over $Mg_3P_2O_8$ and $Mg_2P_2O_7$, satisfactorily correspond to the experimental data obtained by the Knudsen effusion mass spectrometric method in (Lopatin et al., 1986; Lopatin, Semenov, 1989). Higher experimental values of partial pressures of (PO) and (PO_2) gaseous oxides as well as (Mg) over the magnesium phosphates under consideration, are due to the presence of reducing conditions caused by the use of a metal effusion cell.

References

Berak J. (1958) The system magnesium oxide – phosphorus pentoxide. *Roczniki Chem*., vol. 32, no. 1, pp. 17–22.

Demidova S. I., Anosova M. O., Kononkova N. N., Brandstatter F., Ntaflos T. (2019) Phosphorus-bearing olivines of lunar rocks: sources and localization in the lunar crust. *Geochem. Int*., vol. 57, no. 8, pp. 873–892.

Ding G. H., Xie W., Jung I.-H., Qiao Z. Y., Du G. W., Cao Z. M. (2016) Thermodynamic assessment of the MgO–P_2O_5 and CaO–P_2O_5 systems. *Acta Phys.-Chim. Sinica*, vol. 31, no. 10, pp. 1853–1863.

Glushko V. P., Gurvich L. V., Bergman G. A., Veitz I. V., Medvedev V. A., Khachkuruzov G. A., Yungman V. S. (1978–1982) Thermodynamic properties of individual substances. Moscow: Nauka.

Iwase M., Akizuki H., Fujiwara H., Ichise E., Yamada N. (1987) A thermodynamic study of MgO–P_2O_5 slags by means of solid-oxide galvanic cell at 1673 K. *Steel Res*., vol. 58, no. 5, pp. 215–219.

Jung I.-H., Hudon P., Kim W. Y., Van Ende M. A., Rahman M., Curiel G. G. (2013) Thermodynamic database of P_2O_5–containing oxide systems for the dephosphorization process in steelmaking. *High Temp. Mater. Process*, vol. 32, no. 3, pp. 247–254.

Lopatin S. I., Semenov G. A., Kutuzova Y. L. (1986) Mass spectrometric investigation of thermal dissociation of

condensed magnesium phosphates. *Izv. AN SSSR. Neorg. Mater*., vol. 22, no. 9, pp. 1506–1509.
Lopatin S. I., Semenov G. A. (1989) Mass spectrometric investigation of thermal dissociation of alkaline earth metal monophosphates. *Izv. AN SSSR. Neorg. Mater*., vol. 25, no. 4, pp. 645–650.
Lopatin S. I., Shugurov S. M. (2005) Thermochemical study of gaseous salts of oxygen-containing acids: XVII. Magnesium salts. *Russ. J. General Chem*., vol. 75, no. 7, pp. 999–1004.
Oetting F. L., McDonald R. A. (1963) The thermodynamic properties of magnesium orthophosphate and magnesium pyrophosphate. *J. Phys. Chem*., vol. 67, no. 12, pp. 2737–2743.
Shornikov S. I. (2019) Thermodynamic modelling of evaporation processes of lunar and meteoritic substance. *Geochem. Int*., vol. 57, no. 8, pp. 865–872.

Slobodov A. A.[1,4], Shornikov S. I.[2], Radin M. A.[3], Vorozhtsova Yu. S.[4], Ivanova A. N.[4], Efimov R. D.[4] Ensuring of thermodynamic databases efficiency for physico-chemical simulation and calculation

[1] St.-Petersburg State Technological Institute, St.-Petersburg (aslobd@gmail.com)
[2] V. I. Vernadsky Institute of Geochemistry and Analytical Chemistry RAS, Moscow
[3] St.-Petersburg State University of Chemistry and Pharmacy
[4] ITMO University, St.-Petersburg

Abstract. The mathematical apparatus of description, modeling and calculation of thermodynamic functions is given. The main criteria for the completeness and consistency of thermodynamic information have been developed. The effectiveness of the developed databases is illustrated by the results of modeling and calculation of transformations and equilibria for conditions of the ceramic material synthesis (fourteen-component system): SiO_2–K_2O–Na_2O–Al_2O_3–Fe_2O_3–CaO–MgO–TiO_2–P_2O_5–SO_3–H_2O–air.

Keywords: thermodynamics, databases, completeness, consistency, modeling, calculation, transformations, equilibrium, multicomponent nature, ceramics

1. Problems of thermodynamic databases development

There are many problems, the solution of which requires knowledge of the thermodynamic characteristics of substances of various nature. They are especially important in the study of high-component systems with many chemical and phase transformations, where the possibilities of experimental methods are limited and computational and model methods are more promising (Barry, 1988; Carmichael, Eugster, 1992; Kubashewski, Alcock, 1982; Uspensky et al., 2017). However, the information available even in the most serious thermodynamic data systems and reference publications is often very approximate, incomplete, and inconsistent (Glushko et al., 1965–1981; Gurvich et al., 1978–1982; Naumov et al., 1971; Chase, 1998; Robie, Hemingway, 1995; Wagman et al., 1982; Yokokava et al, 1988). This applies both to thermal constants (under standard conditions, 298.15 K, 1 bar) and, in particular, to functional *P*,*T*–dependences, where data are often sparse or absent.

Another aspect of efficiency in creating a database (DB) is associated with the construction of a thermodynamic description of the system and tools under study – determining the range of necessary substances and extracting them from the DB, calculating their thermodynamic characteristics, modeling and calculating transformations and equilibria using the DB (Barry, 1988; Gurvich et al., 1978–1982; Slobodov et al., 2015, 2017).

2. Construction of thermodynamic description of a substance

For a detailed analysis and solution of the problem of developing thermodynamic systems and databases, it is advisable to first consider a set of thermodynamic characteristics necessary to build a complete thermodynamic description of a substance.

It should be noted, firstly, that by determining one or another choice of independent state parameters and the corresponding characteristic functions, various, equivalent to each other, forms of the thermodynamic description of the system are also determined. At the same time, all of them are easily transformed one into another, and any of them equally allows (using the calculation apparatus of thermodynamics of the type and in the spirit of Maxwell's equations, thermodynamic equations of state, etc.) to investigate various properties of both the system as a whole and components, phases and substances that make it up.

From both theoretical and practical points of view, the most convenient choice in constructing such a description is the choice of pressure P and temperature T as independent external parameters of the state. The corresponding characteristic function is then, as is known, the Gibbs energy $G(P,T,n)$ ($n=\{n_i\}$ is the molar composition vector) of the system under study, determined by the chemical potentials μ_i and the content n_i of substances that describe its component and phase composition:

$$G = \sum_i \frac{\partial G}{\partial n_i} n_i \equiv \sum_i \mu_i n_i \qquad (1)$$

In turn, the chemical potential $\mu_i(P,T)$ of the i-th substance is determined through its value $\mu_i°(P,T)$ in the so-called. standard state:

$$\mu_i(P,T) = \mu_i^\circ(P,T) + RT \ln a_i, \qquad (2)$$

where a_i is the activity of the *i*-th substance (relative

to the accepted standard state).

As is known, the most stable phase state under the given (P,T) conditions is usually taken as the standard one for individual substances; for the components of solutions, both a pure substance and a dissolved one. At the same time, due to (1), (2), the quantities μ_i^o are molar (when a pure substance is chosen as a standard) or partial molar (if the standard state is a solution) Gibbs energies $G_i°(P,T)$. Since for carrying out equilibrium calculations it is sufficient to know not the full values of $G_i°(P,T)$ (which are practically impossible to determine), but only their relative changes, the functions of the formation of compounds from the corresponding simple substances are often used as the required "reference scale" – $\Delta_f G°(P,T)$ (hereinafter, the index i of the substance is omitted). It seems more appropriate, but less commonly used, to use as $G°(P,T)$ (i. e., and $\mu°(P,T)$) another, also thermodynamically correct value:

$$G°(P,T) = \Delta_f G°(P_0,T_0) + [G°(P,T) - G°(P_0,T_0)] \quad (3),$$

here P_0, T_0 are respectively the standard values of pressure and temperature, for which the values are currently accepted: P_0 = 1 bar (10^5 Pa), T_0 = 298.15 K (sometimes the old standard is also used P_0 = 1 atm ≡ 101325 Pa, T_0 = 0 K or 293.15 K).

For the enthalpy $\tilde{H}°(P,T)$ and other characteristic functions, the calculation is similar to (3).

Obtaining functions of the type $\tilde{G}°(P,T)$, $\tilde{H}°(P,T)$ does not require, in contrast to $\Delta_f G°(P,T)$, knowledge of the thermodynamic characteristics of simple substances (determining the composition of a given complex) under (P,T)–conditions different from from standard. Since the temperature dependences for the thermodynamic characteristics of substances are most studied at pressures close to the standard one, it is advisable to "tie" the potential $\tilde{G}°(P,T)$ (3) to the value P = P_o, representing the transition from the state (P_0,T_0) to (P,T) first along the isobar: (P_0,T_0) → (P_0,T), then along the isotherm:

(P_0,T) → (P,T):

$$G^o(P,T) - G^o(P_o,T_o) = [G^o(P_o,T) - G^o(P_o,T_o)] + [G^o(P,T) - G^o(P_o,T)] \quad (4).$$

Further substituting (4) into (3) and using the theory and mathematical apparatus of thermodynamics for the components of expression (4), after a series of transformations, it is easy to obtain:

$$\tilde{G}°(P,T) = \Delta_f G°(P_0,T_0) - S°(P_0,T_0)(T - T_0) + \sum_{j=1}^{k}\left[\int_{T_{j-1}}^{T_j} \frac{C_j°(P,t)}{T}\,dT - \int_{T_{j-1}}^{T_j} C_j°(P_0,T)\,dT + \left(\frac{T}{T_j} - 1\right)\Delta H_j°(P_0,T_j)\right] + \int_{P_0}^{P} V°(P,T)\,dP \quad (5),$$

where the last term in (5) corresponds to the second transition in (4) (isotherm), all the previous ones correspond to the first one (isobar). It makes sense to divide thermal constants and functions in (5) into 4 groups:

1. $\Delta_f G°(P_0,T_0) \equiv \Delta_f G_{298}°$, $S°(P_0,T_0) \equiv S_{298}°$ – standard (at P_0 = 1 bar, T_0 = 298.15 K) the Gibbs energy of formation and the entropy of matter, respectively;

2. $T_j \equiv T_{tr}$, $\Delta H_j°(P_0,T_j) \equiv \Delta H_{tr}°$ – are, respectively, the temperatures and standard enthalpies of phase (polymorphic, aggregate, etc.) transformations of matter (if they take place);

3. $C_j°(P_0,t) \equiv C_P°(P_0,t) = \partial H^o/\partial t$ – temperature dependences of isobaric heat capacities for each of the k phases of matter existing in the intervals [T_{j-1}, T_j], (j ∈ 1:k; $T_0 = T_0$, $T_k = T$);

4. $V°(p,T)$ is the baric dependence of the standard molar volume in the interval [P_0, P] at temperature T.

3. Structure and criteria of thermodynamic information quality

Note, firstly, that due to the definition (3) of the functions $G°$, $H°$ (let us denote them below, as well as the usual formation functions, $\Delta_f G°$, $\Delta_f H°$) and the identity $\Delta H = \Delta G + T\Delta S$ (valid for any isothermal changes in the state of the system), for any values of P and T (including standard ones – P_0,T_0) these functions are interconnected by the ratio:

$$\Delta_f H° \quad \Delta_f G° + T\Delta_f S° = \Delta_f G° + T\left(S° \quad \sum_i n_i S_i°\right), \qquad (6)$$

where n_i , $S_i°$ are, respectively, stoichiometric coefficients and standard entropies of simple substances determined by the elemental composition of the compound under consideration.

Expression (5) is a complete thermodynamic description of this substance. From it, as noted above, one can obtain (with some other choice of independent state parameters) other descriptions equivalent to (5), and also calculate all the necessary thermodynamic characteristics (of the type $H = \partial(G/T)/\partial(1/T)$, $S° = -\partial G°/\partial T$, etc.).

Thus, the necessary and sufficient condition for the completeness and correctness of the thermodynamic description of the physicochemical system is the "security" of calculations (5), i.e. the presence for each of the substances included in the system under study, the above four groups of its thermodynamic characteristics.

From here follow the following general criteria (as a whole considered above), characterizing in aggregate the quality of any system or database of thermodynamic data:

1. The degree of chemical completeness - in terms of the substances included in it.

2. The degree of thermodynamic completeness – in accordance with the presence (absence) of data necessary to ensure calculations (5) that satisfy requirement (6).

3. Degree of reliability of thermodynamic data required for calculations (5).

At the same time, in calculation (5), only the influence of its last baric component is taken into account $\int V°(p,T)dp$ does not present (with some reservations) significant difficulties – the molar volume of many individual substances is a relatively simple and well-studied characteristic. Thus, for condensed (solid and liquid) phases, its value $V°(P,T)$ is usually insignificant and relatively weakly depends on temperature and pressure in a fairly wide range. Therefore, the contribution of the baric component to the value $G°(P,T)$ of potential (5) is, as a rule, easily estimated and is often negligible. The behavior of gases in this region is usually close to ideal, and then the well-known equations are applicable (ideal gases $P_iV° = RT$, van der Waals, virial, etc.).

And then for the calculation of (5) the data of the first three groups of thermodynamic characteristics - constants (at standard temperature and at temperatures of phase transformations) and temperature dependences $C_P°(T)$ become decisive. In a practically important special case of conditions close to standard (1 bar, 298.15 K) it is enough to have data only for the first group – thermal constants under standard conditions.

4. Implementation of the developed databases

The above aspects were used in the development of databases of thermodynamic characteristics of individual inorganic substances – for condensed (solid and liquid) and for gaseous states. A database management system (DBMS) was also developed – for procedures for extracting the required set of substances from the database, calculating their thermodynamic characteristics (depending on temperature and pressure), etc.

For each of the condensed substances , the database contains its chemical formula, standard enthalpy $\Delta_f H^o_{298}$ and Gibbs energy of $\Delta_f G^o_{298}$ formation, entropy S^o_{298}, as well as for all phase (aggregate and structural) states - temperature and enthalpy $\Delta_{tr} H^o_T$ for each of the phase (polymorphic or an aggregate (solid – liquid)) transformations, the temperature interval of the existence of this state and the coefficients of the equation $C^o_P(T)$ on this interval. For elements of the "gas base" the data structure is naturally simplified due to the absence of phase transitions.

A set of methods for modeling and calculating the equilibrium compositions of multicomponent systems in a wide range of state parameters (temperature, pressure, composition) has also been developed, where the developed databases are used. The complex has found wide application for studying a number of natural and technological processes in which chemical and/or phase reactions occur. These are, for example, problems of mineralogy and geochemistry, atmospheric phenomena, processes of synthesis of ceramic, glassy, phosphor materials, problems of metallurgy (Slobodov et al., 2015, 2017 , 2021; Uspensky et al., 2017).

As an illustration of the application of the developed databases and modeling methods, the figure shows some results of calculations of the phase-chemical composition of a 14-component inorganic system that simulates the process of synthesis of a ceramic shard from natural raw materials.

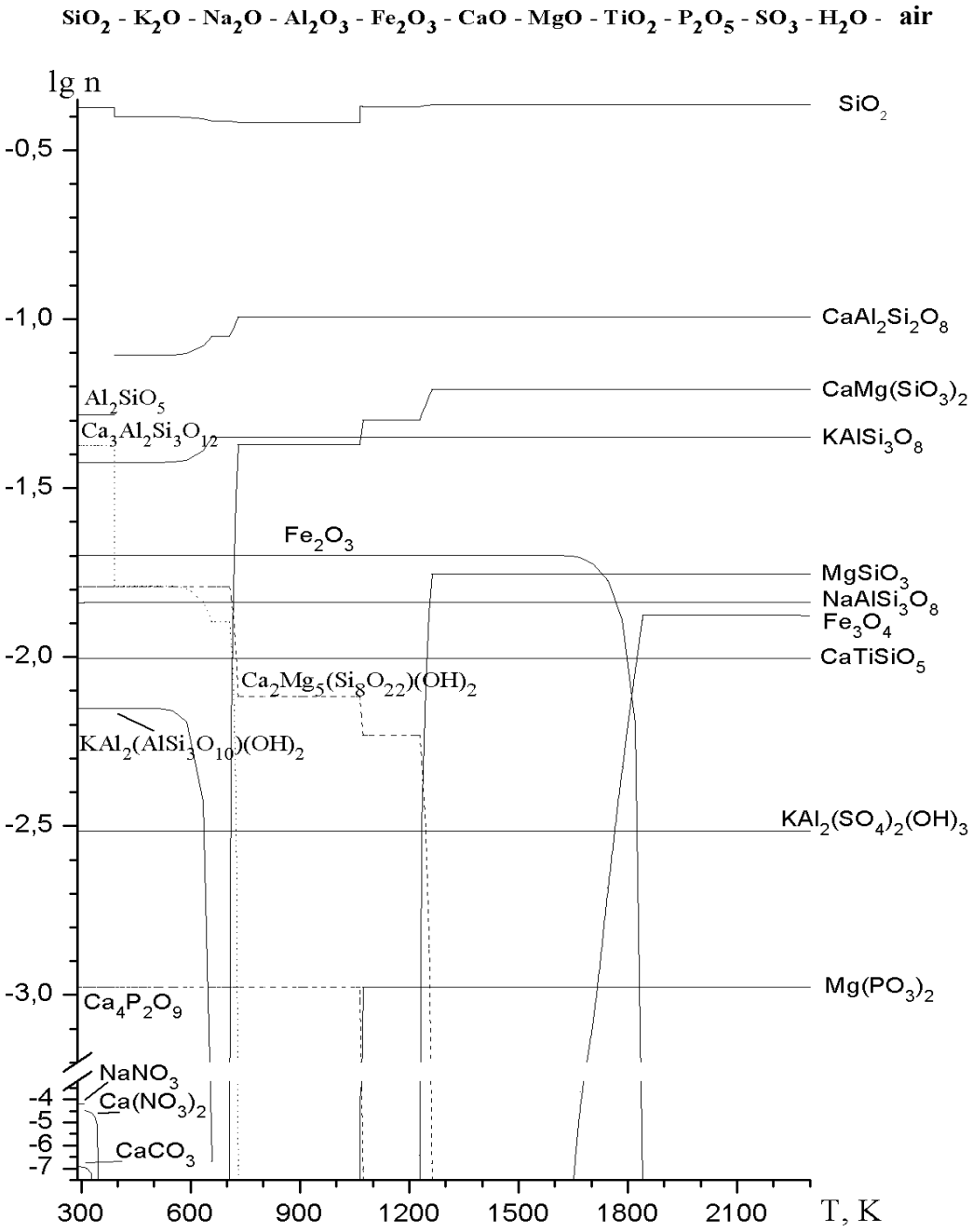

Fig. 1. Influence of temperature on the phase composition of the moisture-containing (0.5%) ceramic mass (lg (mol/kg)) at the boundaries with the gas phase of the interaction products in air-containing pores (10^{-4} m^3/kg).

The data in the figure illustrate the effect of temperature on the phase-chemical transformations occurring in the pore-containing ceramic mass. The results obtained give reasonable answers to the questions – what and in what quantities are phases formed, the temperature conditions for their formation and decomposition, the fields of phase stability, their transformation and chemical interaction, dependence on the composition and atmosphere of synthesis, the formation and composition of gaseous products, etc.

References

Barry T. (1988) Applied chemical thermodynamics. Moscow: Mir.

Carmichael I., Eugster H. (1992) Thermodynamic modeling in geology: minerals, fluids and melts. Moscow: Mir.

Chase M. (1998) NIST-JANAF thermochemical tables. *J. Phys. Chem. Ref. Data,* Monograph no. 9, pp. 1–1961.

Glushko V. P. (1965–1981.) Thermal constants of substances. Moscow: AN SSSR [in Russian].

Glushko V. P., Gurvich L. V., Bergman G. A., Veitz I. V., Medvedev V. A., Khachkuruzov G. A., Yungman V. S. (1978–1982) Thermodynamic properties of individual substances. Moscow: Nauka [in Russian].

Kubashewski O., Alcock S. B. (1982) Metallurgical thermochemistry. Moscow: Metallurgy.

Naumov G. B., Ryzhenko B. N., Khodakovsky I. L. (1971) Handbook of thermodynamic quantities. Moscow: Atomizdat.

Robie R. A., Hemingway B. S. (1995) Thermodynamic properties of minerals and related substances at 298.15 K and 1 bar (10^5 Pascals) pressure and at higher temperatures. *U. S Geol. Surv. Bull*. no. 2131, 492 p.

Slobodov A. A., Uspenskiy A. B., Ralys R., Kremnev D. (2015) Thermodynamic modeling of phase-chemical transformations as the method for study of rheological properties of substances. *J. Sil. Bas. Comp. Mater*., vol. 67, no. 4, pp. 159–163.

Slobodov A. A., Uspenskiy A. B., Yavshits S. G., Lipin V. A., Kritskiy V. G. (2017) Thermodynamic modeling of phase-chemical transformations and equilibrium in multicomponent natural and industrial waters. *WIT Trans. Eng. Sci*., vol. 115, pp. 35–42.

Slobodov A. A., Markov M. A., Krasikov A. V., Bykova A. D., Kravchenko I. N., Kuznetsov Yu. A., Belyakov A. N. (2021) Thermodynamic simulation of microarc oxidation of aluminum and its alloys in aqueous borate electrolytes. *J. Mach. Manuf. Reliab*., vol. 50, no. 8, pp. 83–93.

Uspensky A. B., Ralys R., Kremnev D., Radin M., Slobodov A. (2017) Thermodynamic physico-chemical modelling and calculation for the synthesis process of modern functional materials. *IOP Conf. Series: Materials Sci. Eng*., vol. 175, no. 012024, 6 p.

Wagman D. D., Evans W. H., Parker V. B., Schumm V. B., Halow I., Bailey S. M., Churney K. L., Nuttall R. L (1982) The NBS table of chemical thermodynamic properties. Selected values for inorganic and C_1 and C_2 organic substances in SI units. *J. Phys. Chem. Ref. Data*, vol. 11, suppl. 2, pp. 1–1394.

Yokokawa H., Fujishige M., Ujiie S., Dokiya M. (1988) CTC: Chemical thermodynamic computation system. *J. Nat. Chem. Lab. Ind*., vol. 83, no. 11, pp. 1–122.

Koroleva O.N. Nonlinearity of dynamic and relaxation properties of mixed-alkali silicate glasses

V. I. Vernadsky Institute of Geochemistry and Analytical Chemistry RAS, Moscow olgankoroleva@gmail.com

Abstract. The aim of the study was to determine the structure of non-crystalline silicate glasses containing several alkali cations. A study of silicate glasses containing lithium and potassium in various ratios was carried out. Extremes of the functional dependence of properties on composition when replacing one cation with another are shown to correlate with the distribution of alkaline cations between silicon-oxygen structural units of varying degrees of polymerization.

Keywords: mixed-alkali effect, glass structure, structural units.

One of the important problems concerning the structure of silicate glasses consists in providing an accurate description of the spatial distribution of modifier cations and the ordering of their immediate environment. Traditionally, the locations of such cations were believed to be statistically distributed in the disordered network of a glass near non-bridging oxygen atoms. However, it was subsequently proposed that modifier cations adapt to their local environment by creating coordination polyhedra similar to those observed in crystalline silicates. Such local ordering of the nearest environment of modifier cations is a consequence of the average order in silicate glasses (Gaskell, 1998). Glasses containing two or more modifier cations are characterized by the so-called “mixed alkali effect” (MAE), which is expressed in the nonlinear dependence of the physico-chemical properties of the glass on the cation ratio. A number of authors note that the MAE is manifested not only in terms of changes in ionic conductivity, but also according to other physicochemical properties, such as density, mechanical strength, viscosity, and elasticity.

The aim of the present work is to present a structural description of mixed alkali silicate glasses according to the physico-chemical modeling approach along with a determination of the effect of chemical composition, type of cation modifier, and temperature on the structural features of silicate systems having two or more modifier cations. The physico-chemical modeling approach was successfully applied earlier in order to study the structure of binary silicate, germanate and borate glasses and melts (Koroleva et al., 2021; Koroleva et al., 2022; Koroleva and Shtenberg, 2023). As a result of modeling silicate systems with correction by high-temperature Raman spectroscopy data, information was obtained not only about their structure, but also concerning the distribution of structural units depending on composition and temperature. Additionally, the coordinated thermodynamic characteristics of structural units of glasses and melts were calculated. According to the obtained thermodynamic functions of the components of silicate systems, the structure of Li2O-K2O-SiO2 system was then modelled across a wide range of compositions and temperatures. The universal “Selektor-C” software complex was used as a tool for studying physicochemical processes in silicate melts.

It should be emphasized that not all properties of mixed alkaline glasses exhibit significant deviations from additivity or linearity. In particular, dynamic properties associated with the movement of alkaline cations, such as electrical conductivity and diffusion,

viscosity and chemical resistance, demonstrate the greatest deviations from additivity. This can be seen in Figure 1a, where the change in the molar volume of glass of composition $33(Li_2O+K_2O)\cdot 67SiO_2$ (hereinafter 33(LK)67S) is almost perfectly linear: the density shows small positive and negative deviations from additivity, whereas the deviation from additivity for electrical resistivity is almost five orders of magnitude higher (Day, 1976).

In this regard, the proposed study of the structure of multicomponent melts by physico-chemical modeling is relevant. A composite section having a content of 33 mol % alkali metal oxide 33(LK)67S was studied. The simulation was carried out for a multi-alkaline system in a temperature range up to 1500°C. The formation of a model for a glass-forming mixed alkali system is based on the same principles as those for binary systems.

The list of possible components of the melt model of composition 33(LiK)67Si includes Li_2SiO_3, $KSiO_{2,5}$, $LiSiO_{2,5}$ and K_2SiO_3, whose thermodynamic characteristics correspond to the characteristics of sheet (Q^3) and chain (Q^2) structural units coordinated by lithium or potassium cations. SiO_2 corresponding to the structural units Q^4 present in the melt is additionally taken into account when modeling melt structure of the disilicate composition.

The results of modeling the structure of $(1-x)K_2O\cdot xLi_2O\cdot 2SiO_2$ glass depending on the composition are shown in Figure 1b. It can be seen that, when potassium cations are replaced by lithium cations in glasses containing Q^4, Q^3 and Q^2 structural units, the concentration of Q^4 and Q^2 tetrahedra increases slightly. The obtained data, which are in a good agreement with the results of Raman spectroscopy (Koroleva et al., 2013; Koroleva et al., 2023), are confirmed by calculations (Koroleva et al., 2021): potassium silicate glass of disilicate composition contains more Q^3 tetrahedra than lithium silicate glass of the same composition.

A simultaneous substitution of Q^2(K) for Q^2(Li) and Q^3(K) for Q^3(Li) is observed in the glass structure along with an increase in the Li^+/K^+ ratio. However, it should be noted that, while the content of Q^3(Li) is equal to the same of Q^3(K) in a glass containing 15 mol % of Li_2O, the ratio of chain structural units associated with different types of cations $Q^2(Li)/Q^2(K)$ is greater than three. Such a difference in the distribution of lithium and potassium cations between structural units of different types is certain to affect the possibility of their movement through the formed channels of different sizes.

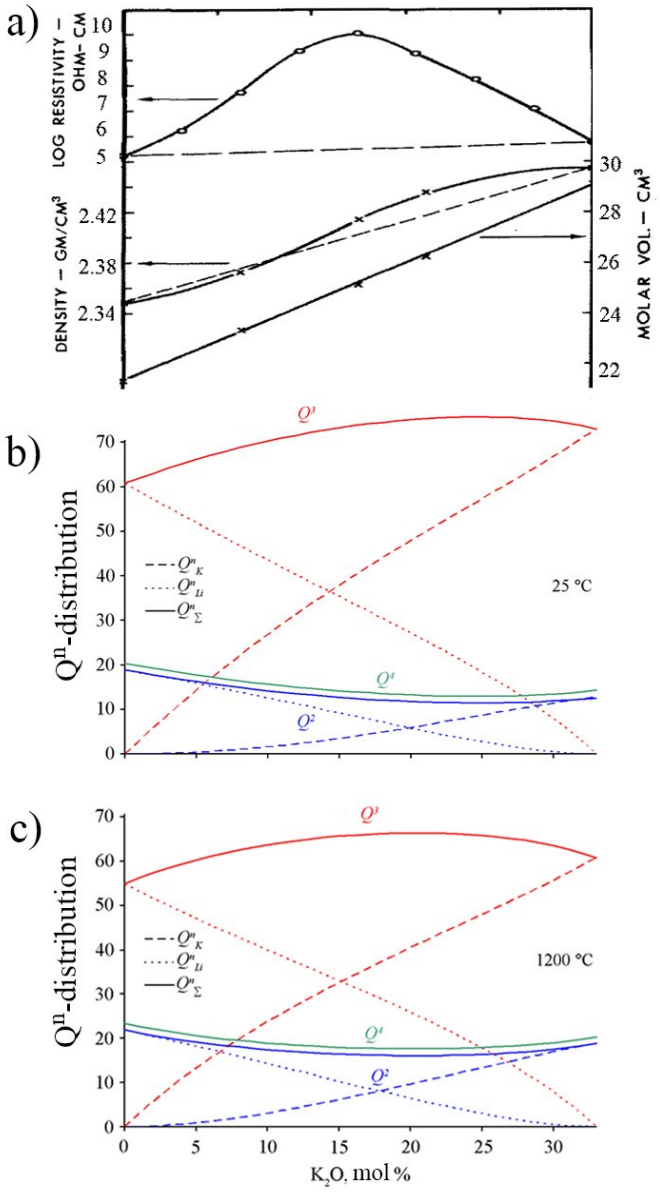

Fig. 1. Dependence of the molar volume, density and resistivity of 33(LK)67S glass on the composition (Day, 1976) (a); distribution of structural units Q^2, Q^3, Q^4 in glass (b) and melt at 1200°C (c) 33(LK)67S depending on the content of potassium oxide.

This conclusion partially agrees with the data obtained by Greaves (Greaves, 1985), who proposed a modified random network (MRN) model. The model is based on the notion that, when two ions of different sizes, such as K^+ and Li^+, share an ion channel, the resultant diffusion is limited by energy factors, since an atom needs more energy to "jump" into the adjacent space recently vacated by an atom of a different size (Greaves et al., 1991). The authors suggest that both the energy and the time needed to adapt to the changing types of sections are responsible for reducing the jump speed. Indeed, as can be seen from Figure 1b, the total number of sheet structural units Q^3(K) and Q^3(Li) in a mixed glass is

greater than in pure potassium silicate glass, which in itself already indicates a deviation of the properties of mixed alkali silicate glass from additivity. This behavior is likely to indicate the ability of Q^3 units to interact with modifier cations in a glass-forming melt at lower temperatures than *Tg* of binary potassium- and lithium-silicate glasses. Thus, the more ordered distribution is probably due to the reduced influence of the entropy factor on the formation of Q^n. The obtained nonlinear dependence on the composition of Q^3 units (to a greater extent), as well as Q^4 and Q^2 units (to a lesser extent), is consistent with the data on the relationship between the decreasing glass transition temperature of mixed glasses with a linear correlation (Bødker et al., 2020).

It is also interesting to note that the maximum dependence of the content of structural units Q^3 does not occur at equal concentrations of two alkaline ions in the glass, but is shifted towards the potassium silicate glass (Figure 1b). This result explains the position of the maximum dependence of the electrical resistance in terms of a function of the difference in the size (mass) of alkaline cations (Day, 1976). Thus, based on our calculations, the most likely reason for the shift of the inflection point of electrical resistance towards a larger cation is the uneven distribution of structural units of the same type between modifier cations characterized by different ionic strengths.

The *effect of temperature on the MAE* can be estimated from comparing the melt and glass structures of three-component K_2O-Li_2O-SiO_2 system. The results of calculating the mixed alkali melt structure of 33(LK)67S composition at 1200ºC are shown in Figure 1c. Here, the ratio of chain units Q^2(Li)/Q^2(K) at the equilibrium point of sheet structural units can be seen to increase to 1.7 with increasing temperature. The indicated increase in disorder in the system should lead to a decrease in the MAE. However, the dependence of the total number of Q^3- units still has a nonlinear positive deviation, whereas the distribution of Q^4 and the sum of Q^2-units has a negative deviation from additivity

Thus, the deviation from the additivity of the dynamic properties of mixed-alkali glasses and melts is obviously related to the selectivity of modifier cations in the distribution between structural units of various types. Modifier cations associated with anionic groups in the melt are in dynamic equilibrium, characterizing the continuous breaking and creation of new cation-anionic complexes. This is to some extent consistent with the polyelectrolyte model, according to which the dynamic equilibrium between cations and anions is described by introducing “free” and “bound” modifier cations

During vitrification, the structure of these individual regions of the melt changes according to the effect of temperature on the structure of each individual binary system. As a result of the modeling of the mixed alkali system depending on temperature, a redistribution of modifier cations between structural units, even those of the same type, was detected. The observed change in the system’s structure when the melt cools down is determined by energy factors. By considering the resulting glass as a union of cationic-anionic regions of various morphologies, it becomes possible to determine their structure according to the proposed and carried-out modeling studies.

Based on the simulation results, chain structural groups $\mathbf{Li}^+K^+Q^2$ represent complexes enriched with lithium cations, whereas sheet structural units containing a predominance of potassium cations can be designated $Li^+\mathbf{K}^+Q^3$. Such an approach may help to explain the observed decrease in cation diffusion and consequent reduction in ionic conductivity when substituting alkaline cations in glass. Accordingly, the narrow channels formed by lithium cations predominating in $\mathbf{Li}^+K^+Q^2$ -type sites can become "clogged up" when more massive potassium cations attempt to move through these channels. Conversely, the larger channels formed by potassium cations in $Li^+\mathbf{K}^+Q^3$-type regions, although predominating in sites of this type, cannot provide greater diffusion of cations than in binary glass. Thus, the formation of conducting channels of different sizes and characteristics in the glass network can be explained in terms of the non-statistical distribution of alkaline cations between silicon-oxygen structural units. The interpretation of the MAE obtained from the simulation results can also help to explain the extremes of the functions of ionic conductivity and other dynamic properties of glass.

The structural modeling of the mixed alkali system explains the temperature dependence of the conductivity and other dynamic properties of glasses in terms of the changing ability of modifier cations to associate with different Q^n tetrahedra upon heating. The results obtained in this work are consistent with the temperature dependencies of the equilibrium constants of reactions between structural units obtained from the values of the Gibbs free energies of the Q^n (Koroleva et al., 2021; Koroleva et al., 2023). All the predicted structures of glasses and melts containing two or more modifier cations were obtained only on the basis of ready-made corrected models of binary glasses and melts of the compositions $Li_2O{-}SiO_2$, $Na_2O{-}SiO_2$ and $K_2O{-}SiO_2$. Therefore, the correction stage taking into account the experimental data from Raman spectroscopy was not carried out for models of three- and four-component systems. The calculated distributions of the main structural groups were used to identify the roles of chain structural units of $\mathbf{Li}^+K^+Q^2$ type

(enriched with lithium cations) and sheet structural units of the $Li^{+}\mathbf{K}^{+}Q^{3}$ type (containing a predominance of potassium cations). The behavior of these structural groups determines the MAE in mixed systems, as well as its dependence on composition and temperature. Consequently, the set of thermodynamic characteristics of structural units previously obtained from binary alkali-silicate models are sufficient to develop a physico-chemical model of multicomponent silicate glass (melt). On the basis of the comparative analysis of the physico-chemical modeling results with the available experimental data, the developed method can be recommended as promising for studying the structure and properties of complex multicomponent oxide melts depending on their composition and external conditions.

References

Gaskell, P.H. The structure of simple glasses. Disorder or order - the debate continues. Physics and Chemistry of glass. 1998. V. 24. P. 266-277.

Koroleva, O.N., Bychinsky, V.A., Tupitcyn, A.A. Thermodynamic modelling of M_2O-SiO_2 (M – Li, Na, K) melts as applying to mixed alkali systems. Journal of Non-Crystalline Solids. 2021. V. 571. P. 121065.

Koroleva, O.N., Shtenberg, M.V., Bychinskii, V.A. Melts and glasses of the K_2O-GeO_2 system: Physicochemical modelling with correction based on the results of Raman spectroscopy. J. Non-Cryst. Solids. 2022. V. 594. P. 121795.

Koroleva, O.N., Shtenberg, M.V., Osipov, A.A. Structural Features of K2O-SiO2 Melts: Modeling and High-Temperature Experiments. Minerals. 2023. V. 13. P. 94.

Day, D.E. Mixed alkali glasses — Their properties and uses. Journal of Non-Crystalline Solids. 1976. V. 21. P. 343-372.

Koroleva, O.N., Anfilogov, V.N., Shatskiy A., Litasov K.D. Structure of Na_2O–SiO_2 melts as a function of composition: in situ Raman spectroscopic study. J. Non-Cryst. Solids. 2013. 375.

Greaves, G.N. EXAFS and the structure of glass. Journal of Non-Crystalline Solids. 1985. V. 71. P. 203-217.

Greaves, G.N., Gurman, S.J., Catlow, C.R.A., Chadwick, A.V., Houde-Walter, S., Henderson, C.M.B., Dobson, B.R. A structural basis for ionic diffusion in oxide glasses. Philosophical Magazine A. 1991. V. 64. P. 1059-1072.

Bødker, M.S., Youngman, R.E., Mauro, J.C., Smedskjaer, M.M. Mixed Alkali Effect in Silicate Glass Structure: Viewpoint of 29Si Nuclear Magnetic Resonance and Statistical Mechanics. The Journal of Physical Chemistry B. 2020. V. 124. P. 10292-10299.

Voronin M.V.[1], Polyakov V.B.[2], Osadchii E.G.[1], Sipavina L.V.[1] Equilibrium iron isotope factors for troilite from mössbauer spectroscopy data: a new evaluating tecnique

UDC 544.582.6

[1]D.S. Korzhinskii Institute of Experimental Mineralogy of Russian Academy of Sciences ; [2]*Vernadsky Institute of Geochemistry and Analytical Chemistry* of Russian Academy of Sciences; *e-mail: voronin@iem.ac.ru*

Abstract. Troilite (FeS) was synthesized and its Mössbauer spectra in the temperature range 90-295 K were obtained. The equilibrium isotope factors (β-factors) of iron troilite were estimated from the temperature shift (TS) in the Mössbauer spectra. The traditional estimation method using the Debye model to describe the ^{57}Fe phonon spectrum in troilite resulted in β-factor values for iron troilite that were significantly different from those determined from nuclear inelastic resonant X-ray scattering experiments. Estimates of the iron β-factor for troilite accounting for anharmonic effects, based on both the Debye model and the Thirring expansion, showed good agreement with the inelastic resonant X-ray scattering data on ^{57}Fe nuclei.

Keywords: troilite; Mössbauer spectra; temperature shift;SOD; the iron β-factor for troilite

For iron isotopes, along with traditional methods of experimental determination of equilibrium fractionation factors (β-factors), it is found possible to use x-ray-resonance methods – nuclear elastic x-ray-resonant scattering (Mössbauer spectroscopy) and nuclear inelastic γ-resonance scattering (NRIXS). In contrast to traditional experimental methods that allow the determination of equilibrium fractionation coefficients between minerals, x-ray-resonance methods make it possible to determine β-factors, which experimental determination was previously considered impossible (Polyakov, 1997; Polyakov et al., 2005b). The equilibrium fractionation factor between to compounds A and B ($\alpha_{A/B}$) is directly expressed through the β-factors of these compounds (β_A and β_B, respectively):

$$\alpha_{A/B} = \beta_A / \beta_B \qquad (1a)$$

The application of first-order thermodynamic perturbation theory allows expressing the β-factor of iron through the kinetic energy of vibrations of the ^{57}Fe nuclei for which the Mössbauer effect is observed. Thus, for the ^{57}Fe/^{54}Fe fractionation, the β-factor can be written in the form (Polyakov, 1997):

$$\ln \beta_{^{57}\mathrm{Fe}/^{54}\mathrm{Fe}} = \frac{m_{^{57}\mathrm{Fe}} - m_{^{54}\mathrm{Fe}}}{m_{^{54}\mathrm{Fe}}} \left(\frac{K_{^{57}\mathrm{Fe}}}{zRT} - \frac{3}{2} \right) \qquad (2)$$

where $m_{^{57}\mathrm{Fe}}$ and $m_{^{54}\mathrm{Fe}}$ are masses of ^{57}Fe and ^{54}Fe nucleuses, respectively; $K_{^{57}\mathrm{Fe}}$ is the vibration kinetic energy of ^{57}Fe per 1 mole; z is the number of iron atoms in the chemical unit; R is the universal gas constant, T is temperature in Kelvins. The use of nuclear x-ray resonant scattering makes it possible to determine the vibrational energy of ^{57}Fe nuclei and thereby evaluate the corresponding β-factor by Eq.

(2). In the case of Mössbauer spectroscopy, the kinetic energy of the vibrations of ^{57}Fe nuclei is expressed through the temperature shift (TS) in Mössbauer spectra due to the second order Doppler (SOD) shift, *i.e.*, changes in the isomer shift, the "center of gravity" of the Mössbauer spectrum with temperature:

$$K_{^{57}\mathrm{Fe}} / z = Sm_{^{57}\mathrm{Fe}}c \quad (3)$$

where S is the SOD shift, expressed in units of the Doppler speed of the source relative to the absorber, c is the speed of light.

Substituting (3) into (2), allows expressing ^{57}Fe/^{54}Fe β-factor through the SOD shift that is can be measured in the Mössbauer experiment:

$$\ln \beta_{^{57}\mathrm{Fe}/^{54}\mathrm{Fe}} = \frac{m_{^{57}\mathrm{Fe}} - m_{^{54}\mathrm{Fe}}}{m_{^{54}\mathrm{Fe}}} \left(\frac{Sm_{^{57}\mathrm{Fe}}c}{RT} - \frac{3}{2} \right) \quad (4)$$

The SOD shift is usually described by the Debye model. In this case, it is expressed using the Mössbauer temperature, θ_M:

$$S(T) = -\frac{9R\theta_M}{8m_{^{57}\mathrm{Fe}}c} \left[1 + 8 \left(\frac{T}{\theta_M} \right)^4 \int_0^{\theta_M/T} \frac{\xi^3}{\exp(\xi) - 1} d\xi \right] \quad (5)$$

In the case of the NRIXS synchrotron experiment, the projection of the vibration density of states (PDOS) on vibration of "Mössbauer isotope" (^{57}Fe for iron) is measured. The vibration kinetic energy of ^{57}Fe can be calculated from its PDOS by the following equation (Polyakov et al., 2007):

$$K_{^{57}\mathrm{Fe}} = \frac{3}{2} RT \int_0^{e_{\max}} E(e,T) g(e) de \quad (6)$$

where $g(e)$ is the PDOS normalized per unity: $\int_0^{e_{\max}} g(e) de = 1$; $E(e)$ is the Einstein function for the energy of a harmonic oscillator of frequency $\nu = e/h$ (h is the Planck constant) at temperature T:

$$E(e,T) \equiv \frac{e/k_B T}{\exp\left(e/k_B T \right) - 1} + 0.5\, e/k_B T \quad (7)$$

k_B in (7) is the Boltzmann constant. Substituting (6) in (2) with (7) allows us to calculate $\ln \beta_{^{57}\mathrm{Fe}/^{54}\mathrm{Fe}}$.

In both Mössbauer spectroscopy and NRIXS, the application of the Thirring expansion by inverse odd degrees of temperature to kinetic energy (Thirring, 1913, 1914; Housley and Hess, 1966) allows us express the β-factor through even moments of PDOS (Polyakov et al., 2005a):

$$\ln \beta_{^{57}\mathrm{Fe}/^{54}\mathrm{Fe}} = \frac{m_{^{57}\mathrm{Fe}} - m_{^{54}\mathrm{Fe}}}{m_{^{54}\mathrm{Fe}}} \sum_{i=1}^{\infty} (-1)^{i+1} \frac{B_{2i}}{2i!} \left(\frac{\theta_{2i}}{T} \right)^{2i} \quad (8)$$

In (8) B_{2i} is the Bernoulli numbers (B_2=1/6, B_4=1/30, B_6=1/42, B_8=1/30, B_{10}=5/66,…), and the characteristic temperature, θ_{2i}, is directly related to the 2i-th moment of PDOS:

$$\theta_{2i} = \frac{1}{k_B} (\mu_{2i})^{1/2i} = \frac{1}{k_B} \left(\int_0^{e_{\max}} g(e) e^{2i} de \right)^{1/2i} \quad (9)$$

In the case of the Debye model, characteristic temperatures are expressed through the Mössbauer temperature (Housley, Hess, 1966):

$$\theta_{2i} = \left(\frac{3}{2i+3} \right)^{1/2i} \theta_M$$

As with traditional methods, equilibrium fractionation factors are considered reliable when the results obtained by different methods match.

The iron β-factors for troilite (FeS) were previously calculated (Polyakov et al., 2007; Polyakov, Soultanov, 2011) based on results of NRIXS experiments (Kobayashi et al. 2004). A subsequent NRIXS experimental study (Polyakov et al., 2013) confirmed both the correctness of the experimental data (Kobayashi et al., 2004) and the iron β-factor calculations (Polyakov et al., 2007) for troilite. In the present study, aimed an estimation of reliability of the previously obtained β-factor values, we determined the iron β-factor for troilite by the Mössbauer spectroscopy technique. In the course of the study, new techniques for processing experimental data were used to evaluate the SOD shift in Mössbauer spectra.

Polycrystalline troilite (FeS) was obtained for the study by dry synthesis (Kullerud, 1971). The presynthesis was carried out by pyrosynthesis, for which stoichiometric amounts of carbonyl iron and elemental sulfur (high purity grade) after homogenization were placed in a quartz glass ampoule and the mixture was ignited. After the reaction, the charge was ground and poured into another ampoule, the ampoule was sealed under vacuum and placed in a horizontal resistance furnace for 14 days at temperature of 700°C. X-ray phase analysis (Bruker D8 ADVANCE diffractometer) showed the presence of only the phase with the structure of troilite.

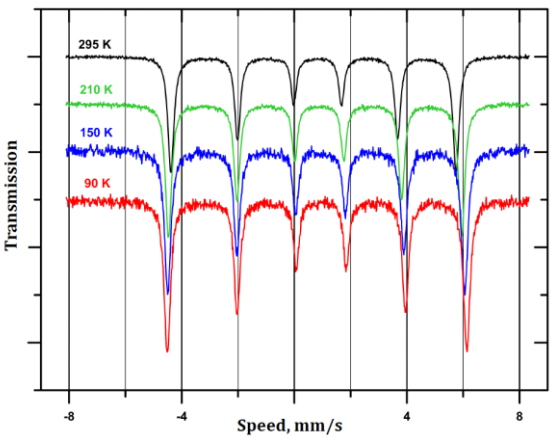

Fig. 1 Mössbauer spectra of troilite (FeS).

The Mössbauer experiment was carried out in the absorption geometry using the MS1104em Mössbauer spectrometer (developed by the Research Institute of Physics, South Federal University, Rostov-on-Don) operating in constant acceleration mode with a triangular form of changing the Doppler speed of the source relative to the absorber. The Mössbauer spectrometer was calibrated at room temperature (22°C) using a standard α-Fe absorber. Mössbauer spectra of troilite were measured in the temperature range between 90 and 295 K. The accuracy of temperature maintenance was ± 0.15 K. The hours. The spectra were processed using the UnivemMS software package (Bruegeman et al., 1993). The obtained spectra are shown in Fig. 1, and the temperature dependences of the isomer shift are presented in Table 1.

Table 1. Temperature dependence of the isomer shift in the Mössbauer spectra of troilite.

Temperature, K	Isomer shift, mm/s			
	Experiment	Unsertainty 1σ	Traditional approach, θ_M =263 K	Considering anharmonicity*, θ_M = 321 K
295	0.7574	0.0002	0.7580	0.7574
270	0.7751	0.0002	0.7755	0.7752
250	0.7886	0.0007	0.7893	0.7893
230	0.8025	0.0006	0.8030	0.8032
210	0.8168	0.0006	0.8165	0.8169
190	0.8304	0.0002	0.8298	0.8303
170	0.8433	0.0006	0.8428	0.8434
150	0.8575	0.0006	0.8555	0.8560
130	0.8682	0.0006	0.8676	0.8679
110	0.8790	0.0020	0.8790	0.8789
90	0.8875	0.0019	0.8901	0.8886

*The anharmonic contribution to temperature dependence of isomer shift is: $-2.691\times10^{-5}T$ (mm/s).

According to usual methodology the temperature dependence of the isomer shift satisfies to the following equation:

$$\delta_{IS}(T) = \delta_0 + S(T) \qquad (11)$$

where, δ_{IS} is the isomer shift, δ_0 is the temperature independent quantity and the SOD shift, $S(T)$, is described by the harmonic Debye model (5). Applying this model to fit the temperature dependence of the isomer shift (Table 1) results in the Mössbauer temperature θ_M = 263 K. Despite the apparently good description of the temperature dependence of the isomer shift (Table 1), the β-factor values for troilite calculated using θ_M = 263 K differ significantly from the results of the NRIXS-based calculations (Polyakov et al., 2007, 2013) (Fig. 2). Since the Debye temperature of troilite is low, anharmonic effects appear at temperatures close to room temperature. This leads to a weak linear dependence of δ_0 on temperature in expression (11) (De Grave, Van Alboom, 1991; De Grave, Eeckhout, 2003). Inserting such an additional term (-2.691×10^{-5} T mm/s) into (11) raises the Mössbauer temperature to θ_M = 321 K. Only one estimate for the Mössbauer temperature, θ_M = 260 K is available from literature (Townsend et al., 1976). Calculations, based on data (Oshtrakh et al., 2016) result in θ_M =316 K.

In tandem with the Debye model, we also processed the experimental results based on the Thirring decomposition. Within this model, the following expression, similar to (8), is valid for SOD:

$$S = -\frac{3}{2}\frac{RT}{mc}\left[1 - \sum_{i=1}^{\infty}(-1)^i \frac{B_{2i}}{(2i)!}\left(\frac{\theta_{2i}}{T}\right)^{2i}\right] \qquad (12)$$

The challenge is reduced to determining the characteristic temperatures θ_{2i}. We added $1.5RT/mc$, to all experimental values of the isomer shift, i.e., added the value of the contribution to the SOD due to classical mechanics, which does not depend on the characteristic temperatures θ_{2i}. We used three terms in Thirring expansion (12) for temperature dependence for the isomer shift. Data obtained at 90 K were not used, since keeping three terms in (12) is not sufficient for correct description of the temperature at this low temperature.

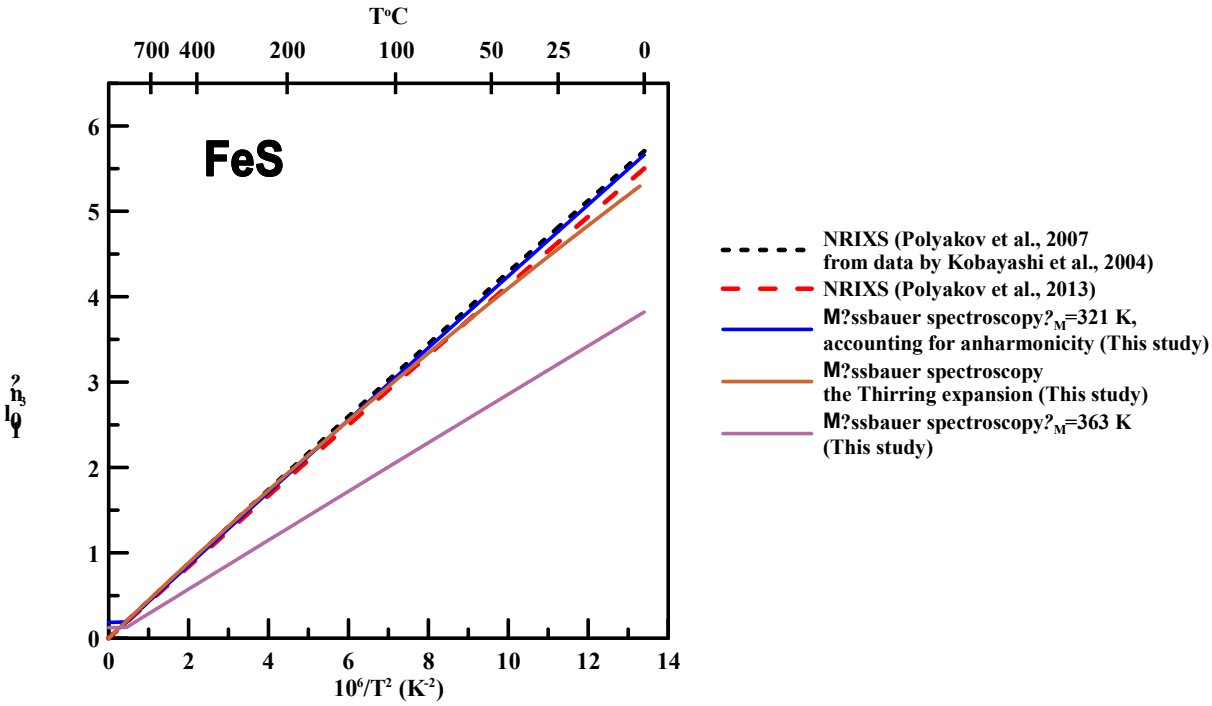

Fig. 2. Comparison of temperature dependences of iron β-factors for troilite obtained by Mössbauer spectroscopy and NRIXS.

We chose as input parameters for the calculation of θ_{2i} all possible differences between increased by $1.5RT/mc$ values of isomer shift. A total of 45 values in the temperature range from 110 to 295 K were selected. The obtained values of characteristic temperatures: θ_2 = 256.3 K; θ_4 = 441.5 K; θ_6 = 489.3 K, allow calculating the $^{57}Fe/^{54}Fe$ β-factors for troilite by equation (8).

Comparison of the found iron β-factor values for troilite with those published earlier (Fig. 2). showed good agreement between the results obtained on the basis of Mössbauer spectroscopy and NRIXS. This allows us to recommend the found values of β-factors for use in geochemical applications. From (4), (8) and (10) after simple transformations we obtain the temperature dependences in the polynomial form:

$$10^3\ln\beta = 0.42921x - 0.52650\times10^{-3}x + 1.00466\times10^{-6}x^3 \quad (13)$$

$$10^3\ln\beta = 0.45615x - 4.39817\times10^{-3}x + 3.78214\times10^{-5}x^3 \quad (14)$$

where $x=10^6/T^2$. Equation (13), which corresponds to the Debye model with θ_M = 321 K, is apparently more reliable, because it agrees better with the literature data.

This study was carried out under government-financed research projects for D.S. Korzhinsky Institute of Experimental Mineralogy of the Russian Academy of Sciences and Vernadsky Institute of Geochemistry and Analytical Chemistry of the Russian Academy of Sciences.

References

Bruegeman S.A., Artsybashev Yu.A., Orlov S.V., "UNIVEM Software", Version 4.50 (MosTek, Rost. Gos. Univ., Rostov on Don, 1993) [in Russian].

De Grave E., Eeckhout S. (2003) ^{57}Fe Mössbauer-effect studies of Ca-rich, Fe-bearing clinopyroxenes: Part III. Diopside. // *American Mineralogist* **88,** 1145–1152.

De Grave E., Van Alboom A. (1991) Evaluation of ferrous and ferric Mössbauer fractions. // *Phys. Chem. Minerals* **18,** 337–342.

Housley R.M., Hess F. (1966) Analysis of Debye-Waller-factor and Mössbauer-thermal-shift measurements. I. General theory. // *Phys. Rev.* **146,** 517–526.

Kobayashi H., Kamimura T., Alfè D., Sturhahn W., Zhao J., Alp E.E. (2004) Phonon density of states and compression behavior in iron sulfide under pressure. *Phys. Rev. Lett.* **93,** 195503.

Kullerud G. (1971) Experimental Techniques in Dry Sulfide Research. In: Ulmer G.C. (eds) Research Techniques for High Pressure and High Temperature. Springer, Berlin, Heidelberg, 288-315.

Oshtrakh M.I., Klencsár Z., Petrova E.V., Grokhovsky V.I., Chukin A.V., Shtoltz A.K., Maksimova A.A., Felner I., Kuzmann E., Homonnay Z., Semionkin V.A. (2016) Iron sulfide (troilite) inclusion extracted from Sikhote-Alin iron meteorite: Composition, structure and magnetic properties. //*Materials Chemistry and Physics*, 174, 100-111.

Polyakov V. B., Osadchii E.G, Chareev D.A., Chumakov A.I., Sergeev I.A. (2013) Fe β-factors for sulfides

from NRIXS synchrotron experiments. // *Mineral. Mag.* **77**, 1985.
Polyakov V.B. (1997) Equilibrium fractionation of the iron isotopes: Estimation from Mössbauer spectroscopy data. //*Geochim. Cosmochim. Acta* **61,** 4213–4217.
Polyakov V.B., Clayton R. N., Horita J., Mineev S.D. (2007) Equilibrium iron isotope fractionation factors of minerals: reevaluation from the data of nuclear inelastic resonant X-ray scattering and Mössbauer spectroscopy. // *Geochim. Cosmochim. Acta* **71**(15), 3833-3846.
Polyakov V.B., Mineev S.D., Clayton R.N., Hu G. (2005a) Oxygen isotope equilibrium factors involving cassiterite (SnO_2): I. Calculation of reduced partition function ratios from heat capacity and X-ray resonant studies. // *Geochim. Cosmochim. Acta* **69,** 1287–1300.
Polyakov V.B., Mineev S.D., Clayton R.N., Hu G. Mineev K.S. (2005b) Determination of tin equilibrium isotope fractionation factors from synchrotron radiation experiments. //*Geochim. Cosmochim. Acta* **69**, 5531–5536.
Polyakov V.B., Soultanov D.M. (2011) New data on equilibrium iron isotope fractionation among sulfides: Constraints on mechanisms of sulfide formation in hydrothermal and igneous systems. // *Geochim. Cosmochim. Acta* **75**, 1957–1974.
Thirring H (1913) Zur Theorie der Raumgitterschwingungen und der spezifischen Wärme fester Körper. *Physik. Z.* **14**, 867-873
Thirring H. (1914) Raumgitterschwingungen und spezifischen Wärme fester Körper. I. //*Phys. Z.* **15**, 127–133.
Townsend M.G., Gosselin J.R., Tremblay R.J., Webster A.H. (1976) Semiconductor to metal transition in FeS. // *Le Journal de Physique Colloques*, 37(C4), C4-11.

Korepanov Ya.I.[1], Chareev D.A.[1], Osadchii V.O.[1], Osadchii E.G.[1] Thermodynamic properties of $(Ag,Pd)_{22}Se_6$ determined by emf method with solid state elelctrolyte in temperature range of 550-723K *UDC 550.4.02*

[1] D.S. Korzhinsky Institute of Experimental Mineralogy of the Russian Academy of Sciences (IEM RAS)
yakoff@iem.ac.ru

Abstract. In the Ag-Pd-Se ternary system, for the equilibrium association Ag_xPd_{1-x}- Ag_2Se- $Ag_{11+y}Pd_{11-y}Se_6$, the temperature dependence of the EMF in an electrochemical cell with a solid electrolyte AgI was determined:
$C|Ag|AgI|(Ag_xPd_{1-x},Ag_2Se, Ag_{11+y}Pd_{11-y}Se_6)|C$
Based on the data obtained and the literature data, the possibility of determination of
1) thermodynamic properties for the phase $(Ag,Pd)_{22}Se_6$
2) activity of silver in a silver-palladium alloy.

Keywords: Thermodynamics, silver, palladium, selenium, chalcogenides, EMF, electrochemistry.

Introduction. Except the native elements Ad, Pd and Se, there are four minerals: palladseite ($Pd_{17}Se_{15}$), verbeekite (monoclinic $PdSe_2$), naumannite (Ag_2Se) and chrisstanleyite ($Ag_2Pd_3Se_4$) in the Ag–Pd–Se system. Minerals of the Ad–Pd–Se system are found in various geological environments. Palladium selenides are known to occur in gold-bearing mineralizations, also known as “jacutinga” type ores, in Minais Gerais and Serra Pelada in Brazil (Clark et.al. 1974, Davis et.al. 1977, Olivo&Gauthier 1995, Cabral et.al. 2002, Cabral&Lehmann 2007) and were observed in carbonaceous Precambrian black shales of the Voronezh crystalline massif in Russia (Rudashevskiy et.al. 1995). Chrisstanleyite was found in gold-bearing carbonate veins in Middle Devonian limestones in Hopes Nose, Torquay, Devon in England (Paar et.al. 1998), and also, as reported, at the Musonoi Cu-Co-Mn-U mine in Shaba province in the Democratic Republic of the Congo (Roberts et.al. 2002), Tilkerode in the East Harz Mountains in Germany (Stanley et.al. 2002), in selenide mineralization in El Chira in Argentina (Paar et.al. 2004), in uranium mineralization in Przedborzice, Czech Republic (Paar et.al. 2005), in the Eastern Pilbara region in Western Australia (Nickel 2002) and in Gongo Soko in Minas Gerais, Brazil (Cabral &Lehmann 2007). Verbeekite is known from the location of its type - the Musonoi Si-Co-Mn-U mine in the Democratic Republic of the Congo (Roberts et.al., 2002) and Hope Nose in Devon in England (Paar et.al., 1998).

Selenides are closely related to sulfides, oxides, tellurides and native elements in various mineral complexes; Se often replaces S in sulfides. Simon (Simon et.al. 1997) examined the mineralogy of selenides in natural ore deposits using thermodynamic data and calculated equilibria for binary selenides presented by Simon&Essene (1996).

Selenides are formed from hydrothermal fluids under conditions of a high fugitivity Se/S. According to Simon et.al. research (1997), an oxidizing medium (close to the anglesite-galena buffer) and Se-rich fluids are necessary for the formation of most selenide minerals. Selenium-rich, relatively reduced (below the hematite-magnetite buffer) hydrothermal fluids can only precipitate Ag selenides; no other selenide minerals can precipitate from such fluids. Selenides are found in four main types of deposits: telethermal selenide veins, uranium deposits associated with inconsistency, uranium deposits in sandstones and epithermal Au-Ag deposits (Simon et.al., 1997). Telethermal deposits of selenide vein type include well-known selenide-containing deposits in the Harz Mountains in Germany (Clausthal, Lerbach, Tilkerode, Trogtal, and Zorge; Tischendorf 1959, Wallis 1994, Stanleyatal. 2002), and in Bolivia (ElDragón, Grund-mann et.al. 1990; Pacajake, E.G., Ahlfeld 1941) and Argentina (the province of La Rioja, for example, Paar et.al. 1996)

The U deposits associated with the discrepancy contain selenide-containing mineralization in the Bohemian Massif (Przedborzice, Petrovice, Habry; Kvaček 1979, Johan, 1989), in the Central Massif in France (for example, Johan et.al., 1982) and in the Athabasca region in Saskatchewan (for example, Robinson 1955). Palladium selenides are known to occur mainly in telethermal selenide veins and U-deposits associated with inconsistency; in these deposits they were formed at low temperatures below 300°C (Simon et.al., 1997).

In this study, an attempt was made to determine the thermodynamic parameters of the $Ag_{11+y}Pd_{11-y}Se_6$ phase (Vymazalova A. et.al., 2014).

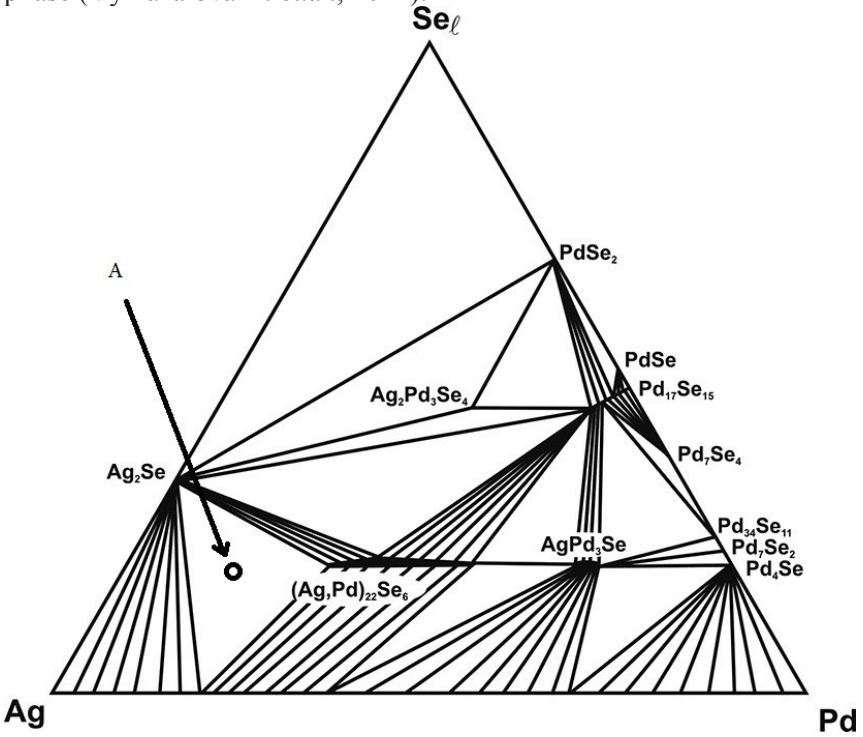

Fig.1. Isothermal section of ternary Ag-Pd-Se phase diagram at T=350 ^oC

Experimental. The composition selected for the study (Ag-0.3762 g, Pd-0.1038 g, Se-0.0688 g) indicated on the Fig.1. (Vymazalova A. et al., 2014). Palladium powder (AldrichChem. Co., 99.95% purity), silver (AldrichChem. Co., 99.99% purity) and selenium (AldrichChem. Co., 99.99% purity) were used to make the sample. The synthesis was carried out in a horizontal furnace in a vacuum ampoule at a temperature of 550 C by two intermediate grindings in an agate mortar to homogenize the composition. AgI (AldrichChem. Co., 99.99% purity) was used as the solid state electrolyte.

The EMF of the element (A) is determined by the difference of the chemical potentials of the element in the sample (the composition is showed Fig.1.) and the pure element.

C|Ag|AgI|(Ag_xPd_{1-x},Ag_2Se, $Ag_{11+y}Pd_{11-y}Se_6$)|C (A)

expected chemical reaction:

$4.54*3Ag_{0.51}Pd_{0.27}Se_{0.22}+5.23Ag=6.77\ Ag_{0.82}Pd0_{0.18}+$
$+Ag_2Se$ (823K)

$4.54*3Ag_{0.51}Pd_{0.27}Se_{0.22}+4.56Ag=6.1\ Ag_{0.8}Pd0_{0.2}+$
$+Ag_2Se$ (623K)

Gibbs energy of reaction:

$\Delta_rG= -nF\boldsymbol{E}(A)/R\boldsymbol{T}$,

n– the number of electrons involved in the reaction, R (universal gas constant) and F(Faraday constant) from IUPAC , *T* the temperature in Kelvins.

To calculate the thermodynamics of the phase, the following values were taken for the Gibbs energy Ag_2Se $\Delta G(\beta\text{-}Ag_2Se)$ =-35062-42.18**T*(Дж/моль) (FengD., TaskinenP., TesfayeF., 2013).

Solid-state electrochemical cell. The schematic of the electrochemical cell (A) for determining EMF is a column of 3 tablets with a diameter of 6 mm and a thickness of 1 to 5 mm. The reference electrode (Ag), the test sample (Ag_xPd_{1-x},Ag_2Se, $Ag_{11+y}Pd_{11-y}Se_6$) and the electrolyte(Ag) between them.

The cell elements (Fig. 2.) are placed in the cell holder (and are compressed by a spring for reliability of electrical contacts. The cell holder is placed in a quartz glass container and then evacuated.

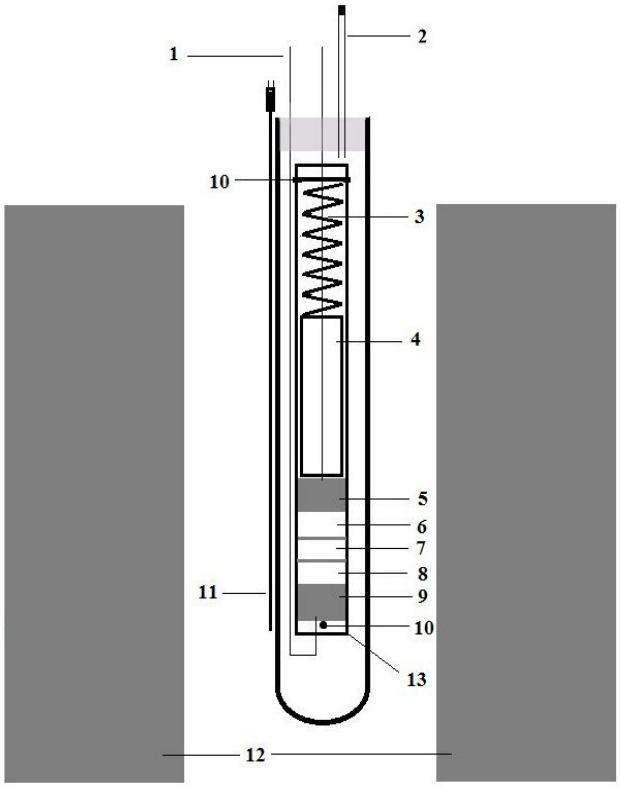

Fig. 2. Schematics of EMF Cell. 1- copper wires, 2- vacuum tube, 3 – spring, 4- quartz tube, 5- graphite plate, 6 – sample, 7 – AgI solid electrolyte, 8- Ag comparison sample, 9- graphite plate, 10 – ceramic stopper, 11 – thermocouple, 12 – furnace, 13 – quartz cell body.

Results. Temperature dependence of (E, mV) shown Fig.1.

E(mV)=-33,65+0.0802*T*(K)

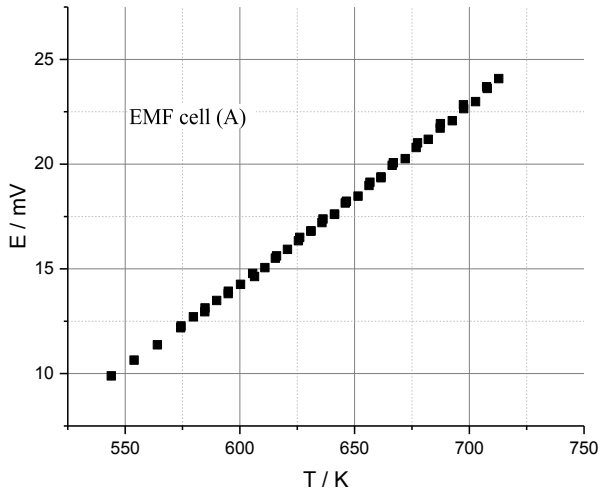

Fig.3. EMF dependence cell (A)

Conclusions. Comparing the obtained EMF dependence with the existing data (Fig.4.) and considering the investigated ternary association Ag_xPd_{1-x}- Ag_2Se- $Ag_{11+y}Pd_{11-y}Se_6$, it can be assumed that at a fixed temperature in the electrochemical cell (A), the activity of silver in the alloy and the hypothetical reaction are simultaneously measured:

$4.54*3Ag_{0.51}Pd_{0.27}Se_{0.22}+5.23Ag=6.77\ \ Ag_{0.82}Pd0_{0.18}+Ag_2Se$ (823K)

$4.54*3Ag_{0.51}Pd_{0.27}Se_{0.22}+4.56Ag=6.1\ \ Ag_{0.8}Pd0_{0.2}+Ag_2Se$ (623K)

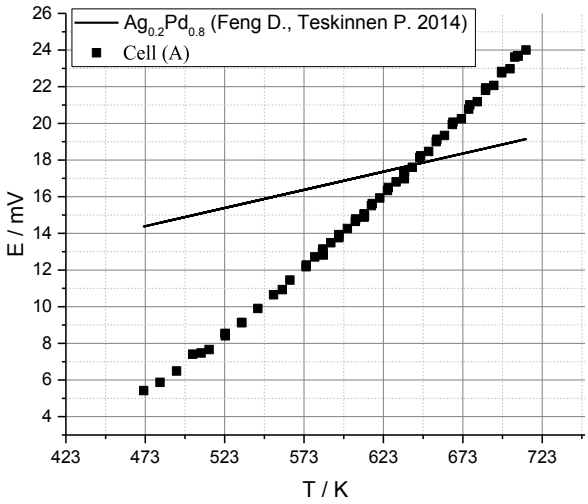

Fig.4. Comparison of the obtained data with the literature (FengD., TaskinenP. 2014)

In the studied temperature range, the alloy composition varies from Ag0.8Pd0.2(623 K) to Ag0.78Pd0.22 (823 K). Adjusted for the error (both our data and those given by Taskinen), we assume that at T=623 K the dependencies intersect, which fully confirms with our assumption.

Thus, for our calculations, we can assume that

$\Delta G_f(Ag_{0.82}Pd0_{0.18})$= -3923.1(J/mol) (823K)(Feng D., Taskinen P., 2014)

$\Delta G_f(Ag_{0.8}Pd0_{0.2})$= -3643.3(J/mol) (623K) (Feng D., Taskinen P., 2014)

$\Delta G_f\ (Ag_{0.51}Pd_{0.27}Se_{0.22})=(5.23*F*E+\Delta G_f\ (Ag_2Se)+6.77\Delta G_f(Ag_{0.82}Pd0_{0.18}))/4.54$

$\Delta G_f\ (Ag_{0.51}Pd_{0.27}Se_{0.22})=(4.56*F*E\ +\Delta G_f\ (Ag_2Se)+6.1\Delta G_f(Ag_{0.8}Pd0_{0.2}))/4.54$

Accordingly:

$\Delta G_f(Ag_{0.51}Pd_{0.27}Se_{0.22})$=-10636.8-2.98**T*(J/mol)

Acknowledgments. This work is fulfilled under Research program № FMUF-2022-0002 of the Korzhinski Institute of Experimental Mineralogy and of leading scientific schools of the Russian Federation within the framework of the project "Chalcogenides: crystal growth, geochemistry, thermodynamics and physical properties" (NSH-2394.2022.1.5).

References

Ahlfeld, F. (1941) El yacimiento de selenio de Pacajake. Ministerio de la Economia Nacional BoletinInformativo, La Paz, Bolivia 1(2), 23–28.

Cabral, A.R., Lehmann B., Kwitko R., Galbiatti H.F., & Pereira M.C. (2002) Palladseite and its oxidation: evidence from Au-Pd vein-type mineralization (jacutinga), Cauê iron-ore mine, Quadrilátero Ferrífero, Minas Gerais, Brazil. Mineralogical Magazine 66(2), 327–336.

Cabral A.R., Lehmann B. (2007) Seleniferous minerals of palladium and platinum from ouropreto-bearing mineralization in Brazil. Ore Geology Reviews 32, 681–688.

Clark A.M., Criddle A.J., Fejer E.E. (1974) Palladium arsenide-antimonides from Itabira, Minas Gerais, Brazil. Mineralogical Magazine 39, 528–543.

Davis R.J., Clark A.M., Criddle A.J. (1977) Palladseite, a new mineral from Itabira, Minas Gerais, Brazil. Mineralogical Magazine. 41(123), M10–M13.

Feng D., Taskinen P. Thermodynamic properties of silver–palladium alloys determined by a solid state electrochemical method, Journal of Materials Science. – 2014. – T. 49. – C. 5790-5798.

Feng D., Taskinen P., Tesfaye F. Thermodynamic stability of Ag2Se from 350 to 500 K by a solid-state galvanic cell, Solid State Ionics. – 2013. – T. 231. – C. 1-4.

Grundmann G., Lehrberger G., Schnorrer-Köhler G. (1990) The El Dragón mine, Potosi, Bolivia. Mineralogical Record 21, 133–146.

Johan, Z. (1989) Merenskyite, $Pd(Te,Se)_2$, and the low-temperature selenide association from the Předbořice uranium deposit, Czechoslovakia. NeuesJahrbuch für Mineralogie (Monatshefte) 4, 179–191.

Johan Z., Picot P., Ruhlmann, F. (1982) Evolution paragénétique de la mineralisationuranifere de Chameane (Puy-de-Dome), France: Chameanite, geffroyite et giraudite, trois seleniures nouveaux de Cu, Fe, Ag et As. TschermaksMineralogische und Petrographische Mitteilungen 29, 151–165.

Kvaček M. (1979) Selenides from the deposits of western Moravia, Czechoslovakia. Acta Universitatis Carolinae-Geologica 1(2), 15–38

Nickel E.H. (2002) An unusual occurrence of Pd, Pt, Au, Ag and Hg minerals in the Pilbara Region of Western Australia. Canadian Mineralogist 40, 419–433.

Olivo G.R., Gauthier M. (1995) Palladium minerals from the Cauê iron mine, Itabira district, Minas Gerais, Brazil. Mineralogical Magazine 59, 455–463.

Paar W.H., Roberts A.C., Criddle A.J., Topa D. (1998) A new mineral, chrisstanleyite, Ag2Pd3Se4, from Hope`s Nose, Torquay, Devon, England. Mineralogical Magazine 6, 257–264.

Paar W.H., Topa D., Makovicky E., Culetto,F.J. (2005) Milotaite, PdSbSe, a new palladium mineral species from Předbořice, Czech Republic. Canadian Mineralogist 43, 689–694.

Paar W.H., Sureda R.J., Brodtkorb M.K. (1996) Oro y plataenlosyacimientos de selenio de La Rioja, Argentina: hallazgo de fischesserita, Ag3AuSe2. III Reunion de Mineralogía y Metalogenia. Publicación del Instituto de RecursosMinerales (Universidad Nacional de la Plata) 5, 177–185.

Paar W.H., Topa D., Makovicky E., Sureda R.J., Brodtkorb M.K., Putz H. (2004) Jaqueite, $Cu_2Pd_3Se_4$, a new mineral species from El Chire, La Rioja, Argentina. Canadian Mineralogist 42, 1745–1755.

Roberts A.C., Paar W.H., Cooper M.A., Topa D., Criddle A.J., Jedwab J. (2002) Verbeekite, monoclinic PdSe2, a new mineral from the Musonoi Cu-Co-Mn-U mine, near Kolwezi, Shaba Province, Democratic Republic of Congo. Mineralogial Magazine 66(1), 173–179.

Robinson S.C. (1955) Mineralogy of uranium deposits, Goldfields, Saskatchewan. Geological Survey of Canada Bulletin 31, 128p.

Rudashevskiy N.S., Knauf V.V., Chernyshov N.M. (1995) Platinum-group minerals from Kurs magnetic anomaly black shales. DokladyAkademiiNauk 344(1), 91–95.

Stanley C.J., Criddle A.J., Lloyd D. (1990) Precious and base metal selenide mineralization at Hopes Nose, Torquay, Devon. Mineralogical Magazine 54, 485–493.

Stanley C.J., Criddle, A.J., Förster H.J., Roberts, A.C. (2002) Tischendorfite, $Pd_8Hg_3Se_9$, a new mineral species from Tilkerode, Harz Mountains, Germany. Canadian Mineralogist 40, 739–725.

Simon G., Kesler S.E., Essene E.J. (1997) Phase relations among selenides, sulphides, tellurides, and oxides: II. Applications to selenide-bearing ore deposits. Economic Geology 92, 468–484.

Simon G., Essene E.J. (1996) Phase relations among selenides, tellurides, and oxides. I. Thermodynamic properties and calculated equilibria. Economic Geology 92, 468–484.

Tischendorf G. (1959) Zur Genesis einiger Selenid-vorkommen, insbesondere von Tilkerodeim Harz. Freiburg Forschungshefte Hamburg C208.

Vymazalová A. et al. The Ag–Pd–Se system: phase relations involving minerals and potential new minerals, The Canadian Mineralogist. – 2014. – T. 52. – №. 1. – C. 77-89.

Wallis E. (1994) Erzparagenetische und mineralchemische Untersuchung der Selenide in Harz. Unpublished Diploma thesis, University of Hamburg, Hamburg, Germany.